

Evolution of a Florida Cirrus Anvil

T. J. Garrett¹, B. C. Navarro¹, C. H. Twohy¹¹, E. J. Jensen³, D. G. Baumgardner², P. T. Bui³, H. Gerber⁴, R. L. Herman⁵, A. J. Heymsfield⁶, P. Lawson⁷, P. Minnis⁸, L. Nguyen⁸, M. Poellot⁹, S. K. Pope¹⁰, and E. M. Weinstock¹², F. P. J. Valero¹⁰

¹Meteorology Department, University of Utah, USA

²Universidad Nacional Autonoma de Mexico, Mexico

³NASA Ames Research Center, USA

⁴Gerber Scientific, Inc., USA

⁵Jet Propulsion Laboratory, California Institute of Technology, USA

⁶National Center for Atmospheric Research, USA

⁷SPEC, Inc., Boulder, Colorado, USA

⁸NASA/Langley Research Center, USA

⁹Department of Atmospheric Sciences, University of North Dakota, USA

¹⁰Scripps Institution of Oceanography, USA

¹¹College of Oceanic and Atmospheric Sciences, Oregon State University, USA

¹²Harvard University, USA

Short title: EVOLUTION OF A FLORIDA CIRRUS ANVIL

Abstract. This paper presents a detailed study of a single thunderstorm anvil cirrus cloud measured on 21 July 2002 near southern Florida during the Cirrus Regional Study of Tropical Anvils and Cirrus Layers-Florida Area Cirrus Experiment (CRYSTAL-FACE). NASA WB-57F and University of North Dakota Citation aircraft tracked the microphysical and radiative development of the anvil over three hours.

Measurements showed that the cloud mass advected downwind from the thunderstorm was separated vertically into two layers: a cirrus anvil with cloud top temperatures of -45°C that lay below a second, much more tenuous layer at the tropopause with temperatures near -70°C . In both cloud layers, ice crystals smaller than $50\text{ }\mu\text{m}$ across dominated the size distributions and cloud radiative properties. In the anvil, ice crystals larger than $50\text{ }\mu\text{m}$ aggregated and precipitated while small ice crystals increasingly dominated the size distributions; consequently, measured ice water content and ice crystal effective radii decreased with time. Meanwhile, the anvil thinned vertically, maintaining a similar stratification to its environment. Analysis of the anvil dynamics suggests the thinning was driven by concentrated heating and cooling at the anvil top and base, in layers $\sim 100\text{ m}$ thick where cloudy air was forced laterally. Unlike the anvil, the thin tropopause cirrus layer spread but did not dissipate. Radiative transfer calculations suggest this was because the anvil shielded the tropopause cirrus from terrestrial infrared heating. Top-of-troposphere radiative forcing above the anvil and TTC was initially strongly cooling, but it decreased with time as the cloud became more tenuous.

1. Introduction

The anvil cirrus outflow from low-latitude cumulonimbus clouds is an important component of the earth's climate, for its role in moistening the upper troposphere, and its perturbation to atmospheric fields of solar and terrestrial radiative fluxes. There is an increasing realization that numerical simulations of low-latitude climate require detailed implementation of detailed cloud microphysics schemes (e.g. Iacobellis and Somerville, 2000). However, there have been relatively few *in situ* measurements that can be used to guide these computations. This is largely due to the logistic difficulties associated with flying aircraft in low-latitude anvil cirrus: these clouds are high, cold and often remote.

The few airborne studies of low-latitude cirrus anvils (Griffith et al., 1980; Knollenberg et al., 1982; Knollenberg et al., 1993; McFarquhar and Heymsfield, 1996; Heymsfield et al., 1998) have shown, for example, that low-latitude cirrus anvil ice water content (*IWC*) is horizontally variable, decreases with increasing height, and can range from a few hundredths of a gram per cubic meter to over a tenth of a gram per cubic meter; due to ice crystal sedimentation and aggregation, large ice crystals are most common near the base of an anvil, where sizes larger than $1000\ \mu\text{m}$ are not uncommon; near the anvil top, concentrations of ice crystals with sizes smaller than $< 100\ \mu\text{m}$ might exceed $100\ \text{cm}^{-3}$; and large precipitating crystals near cloud base contribute most highly to the solar albedo of the cloud.

However, these early studies had several limitations. In most, fields of cloud mass and optical extinction were not measured directly but rather estimated from integration of ice crystal size distributions. Although this was unavoidable given the available instrumentation, such integration required some simplistic assumptions about crystal habit and density. Also, either instrument

uncertainty or lack of instrumentation limited confident measurement of the concentrations of ice crystals smaller than approximately $50\ \mu\text{m}$ diameter. And aircraft were often unable to reach the extreme upper portions of low-latitude anvils where ice crystals tend to be smallest, and where they are most radiatively important due to their more direct exposure to outer space. Finally, anvils clearly develop as they detrain from convection, but in none of these studies was this evolution probed in detail.

This paper attempts to address these limitations using data obtained during the Cirrus Regional Study of Tropical Anvils and Cirrus Layers-Florida Area Cirrus Experiment (CRYSTAL-FACE), which focused on anvil cirrus over Southern Florida. It provides a detailed case study of the evolution of a single low-latitude cirrus anvil sampled over three hours on 21 July 2002. The anvil was chosen from others studied during CRYSTAL-FACE because it was isolated from surrounding convection and it was well characterized by two aircraft *in situ*. These two aircraft were outfitted with an unusually wide range of microphysical, meteorological and radiation probes, many of which were flown in anvil cirrus for the first time.

2. Meteorological overview

A thunderstorm formed over the west coast of Florida in the afternoon of 21 July 2002. No significant synoptic systems were in the storm development region. Instead, diurnal heating over the peninsula and general light southerly low-level flow enabled a north to south sea breeze front to develop over the west coast of Florida by early afternoon. This sea breeze front is evident on satellite images centered on the storm development region (Fig. 1a). Nearby soundings showed values of convective available potential energy (CAPE) near $1000\ \text{J kg}^{-1}$. This CAPE value is only about half the mean value of $2458\ \text{J kg}^{-1}$ found in the region during the latter

half of CRYSTAL-FACE. However, it is within 15% of mean values observed during other low-latitude field campaigns such as TOGA-COARE, which took place over the western Pacific warm pool, and within the range of $660\text{--}1190\text{ J kg}^{-1}$ measured for GATE, which took place over the tropical Atlantic (Li, 2003). Low-level convergence along the sea breeze front combined with the convective instability to initiate storm development over the southwest Florida peninsula at about 1700 UTC, with anvil development occurring subsequently at about 1815 UTC (Fig. 1b). A sounding was taken on Florida's west coast at $25^{\circ}53'\text{N } 81^{\circ}19'\text{W}$, $\sim 12\text{ km}$ west of the sea breeze front and $\sim 35\text{ km}$ southeast of the storm development location. The sounding indicates the region was characterized by $15\text{ to }20\text{ m s}^{-1}$ northeasterly winds at 200 mb (Fig. 2). Consequently, the anvil trajectory at this level was to the southwest over the open waters of the Gulf of Mexico, and in the opposite direction of the movement of the storm (Fig. 1c). The storm reached a peak intensity at 1750 UTC, with radar reflectivities near 50 dBZ, and remained near peak intensity until 1840 UTC when it began to weaken. Most of the resulting cloud mass then relaxed to what was presumably its level of neutral buoyancy at about 11 km altitude. NASA S-band polarimetric radar (N-POL) imagery showed an outflow boundary nearer the surface that propagated to the east away from the storm, and peak reflectivities decreased to less than 40 dBZ. Meanwhile, the anvil spread southwest over the Gulf, and by 1945 UTC, it separated from the dissipating storm.

Figure 1

Figure 2

3. Measurement techniques

3.1. Airborne platforms

The majority of the aircraft measurements were carried out during the dissipating stages of the storm between 1945 and 2145 UTC, with a few measurements taken while the anvil was still

developing between 1845 and 1945 UTC. Measurements were closely representative of a single system since the storm was sufficiently small to be isolated from adjacent convection. In this study, only data from instruments mounted on the NASA WB-57F and the University of North Dakota (UND) Citation Cessna II aircraft are used. Maximum altitudes attained by each aircraft on 21 July were ~ 15.7 km and ~ 12.0 km, respectively, while the average flight airspeed of both aircraft was ~ 140 m s $^{-1}$. Specific instruments located on each aircraft are discussed in the following section.

3.2. Instrumentation

3.2.1. Ice crystal sizes and shapes

On the Citation, a Particle Measuring System's (PMS) Forward Scattering Spectrometer Probe (FSSP-100), a PMS OAP 2D-C probe, and a Stratton Park Engineering Company, Inc. (SPEC) High Volume Precipitation Spectrometer (HVPS) measured the combined size range of ice crystals from 4 to 27000 μm diameter. Aboard the WB-57F, a Droplet Measurement Technologies (DMT) Cloud Aerosol Precipitation Spectrometer (CAPS) was used to measure size distributions of particles between 0.5 and 1550 μm diameter (Baumgardner et al., 2002). The CAPS probe is actually a combination of the Cloud Aerosol Spectrometer (CAS) (which sizes particles smaller than 50 μm) and the Cloud Imaging Probe (CIP) (which images particles larger than 25 μm). The CAS works on principles similar to the FSSP-100, and the CIP is similar to the OAP 2D-C, except that it has an extended size range and updated electronics.

Since the 2D-C has a restricted sample volume for small crystal sizes, FSSP-100 data are used in this study for the size range between 25 and 62 μm covered by both instruments. Ice crystals between 10 to 500 μm were imaged on both aircraft using a SPEC Cloud Particle Imaging

probe (CPI) (Lawson et al., 2001), which has a nominal $2.5 \mu\text{m}$ resolution. In the CPI, ice crystals pass through an intersection of two lasers. The instrument then images the ice crystal with a third laser pointed toward a digital camera.

3.2.2. Bulk microphysical properties

Bulk microphysical probes on the Citation and WB-57F did not measure individual ice crystals, but instead the integral properties of ice crystal populations. The three bulk quantities measured on both aircraft were the optical extinction coefficient β_{ext} , the ice water content IWC , and the asymmetry parameter g . Measurements of β_{ext} and g are used in radiative transfer models to estimate cloud radiative fluxes. The value of g indicates the degree of forward versus back-scattering by ice crystals, while β_{ext} represents the optical cross-sectional density. It is more simple, and ostensibly more accurate, to obtain the bulk quantities g , β_{ext} and IWC from bulk probes rather than from size distributions of cross-sectional areas, habits, and densities of individual ice crystals: fewer assumptions about ice crystal shape are required.

Both the Citation and WB-57F used a Gerber Scientific, Inc. Cloud Integrating Nephelometer (CIN) (Gerber et al., 2000) to measure β_{ext} . The CIN detects 635 nm laser light scattered by ice crystals into four integrating Lambertian sensors, with an angular domain of 10° to 175° . The fraction of light scattered outside the CIN angular domain is estimated to be 0.57 ± 0.02 (Gerber et al., 2000). This value is closely constrained because forward diffraction is half of scattered energy for particles large with respect to the wavelength of light. Both CINs had large sampling volumes of $\sim 0.5 \text{ m}^3 \text{ s}^{-1}$. The lowest value of β_{ext} reliably detected was approximately 0.4 km^{-1} aboard the WB-57F and about 1.0 km^{-1} aboard the Citation, but with approximately 40% error due to extraneous light leakage and photomultiplier shot noise. In clouds approximately twice

as optically thick, the error is estimated to be about 15%. The CIN aboard the Citation obtained the asymmetry parameter g at visible wavelengths with an estimated uncertainty of ± 0.02 in clouds where $\beta_{ext} > 10 \text{ km}^{-1}$. Garrett et al. (2001) give a detailed description of error analysis techniques applied to CIN data.

Bulk IWC was obtained using a Harvard Lyman-Alpha Total Water probe aboard the WB-57F and a counterflow virtual impactor (CVI) aboard the Citation. The Harvard Lyman-Alpha Total Water instrument uses an inlet heater to evaporate ice crystals and a 121.6 nm radiation lamp to photo-dissociate water vapor. The fluorescence of the resulting OH molecules, detected in a photomultiplier tube, is proportional to the water vapor volume mixing ratio. Ice water content is then derived by subtracting out water vapor from total water. A full description of this instrument has been given in Weinstock et al. (1994). The CVI impacts cloud ice crystals and water drops into dry nitrogen gas, where the crystals and drops evaporate (Noone et al., 1988). The water vapor resulting from the evaporating drops and ice crystals is then measured using a Lyman-alpha absorption hygrometer (Buck, 1985; Twohy et al., 1997). The estimated accuracy for both measurements of IWC is approximately 15%.

In the past, the ice crystal effective radius r_e , which is important in radiative transfer calculations for parameterizing cloud scattering and absorption, has normally been derived from measurements of ice crystal size spectra. This requires assumed mass, area, and length relationships for ice crystals. Here we circumvent these issues using direct measurements of β_{ext} and IWC , from which r_e is derived using

$$r_e = \frac{3IWC}{2\rho_i\beta_{ext}} \quad (1)$$

(Foot, 1988; Garrett et al., 2003), where ρ_i is the bulk density of ice. Eq. 1 is general for all possible distributions of ice crystal shape and size.

3.2.3. Meteorological and satellite measurements

Aboard the WB-57F, meteorological state variables, such as temperature, pressure, and wind velocity were measured using the Meteorological Measurement System (MMS) (Scott et al., 1990). Relative humidity was measured using the Jet Propulsion Laboratory (JPL) Laser Hygrometer (May, 1998). The JPL Laser Hygrometer uses a near-infrared diode laser to detect water vapor. On the Citation, temperature and pressure were measured with a Rosemount Total Temperature probe (Payne et al. 1994) and a Rosemount Static Pressure Transducer. Wind velocity was obtained using the Citation's airspeed, ground speed, and the aircraft's Position and Orientation System (POS) (Khelif et al., 1999). Relative humidity measurements were obtained using a tunable diode laser (TDL). The estimated accuracy of the TDL is 5%.

Broadband flux for the shortwave and infrared radiative fields was measured aboard the WB-57F using the Radiation Measurement System (RAMS) (Valero et al., 1997). This system uses radiometers to measure both upwelling and downwelling radiation.

In addition to the airborne instruments, this study uses GOES-8 Visible Infrared Solar Infrared Split Window Technique (VISST) derived cloud products matched to the flight tracks of each aircraft (Minnis et al., 1995; Minnis et al., 1998). These products are derived from a weighted average of the four closest pixels to the aircraft position.

3.3. Aircraft flight patterns

Aircraft flight patterns were coordinated so that the WB-57F sampled the extreme upper portions of the anvil while the Citation sampled the middle and lower portions. Nine level flight legs were completed by the WB-57F and six by the Citation (Fig. 3). The WB-57F flew across the anvil axis for legs 1 to 3, then along most of the length of the anvil axis at an angle of about 35° for the remainder of the legs. The Citation flew at an angle of approximately 35° to the anvil axis, stopping in the center portion of the anvil.

In addition to the horizontal transects, a spiral ascent profile was completed by each aircraft (Fig. 1c), with the WB-57F displaced about 15 km to the southwest of the Citation. The Citation's maximum altitude for the vertical profile was about 11.3 km while the WB-57F profile extended from 12.9 km to 15 km. Thus, an approximate vertical gap of 1.6 km separated the upper profiles of the two planes. This makes it difficult to ascertain with certainty the total depth of the cloud. However, flight notes from the WB-57F remarked on the presence of two cloud layers. Also, the GOES-8 satellite retrieved a cloud top height of ~ 11.0 km for the anvil, which is similar to the maximum cloud height of 11.3 km measured by the Citation. This suggests the Citation profiled the entire vertical depth of a cloud layer, which we call the anvil proper, that was distinct and much thicker than a higher cloud layer sampled by the WB-57F. We believe this second layer sampled by WB-57F during legs four to nine was separated vertically from the anvil proper by >1 km. The exact origin of this tropopause cloud is not clear. However, based on satellite retrieved cloud top height and N-POL radar time-height cross sections, it appears the WB-57F sampled near the storm's second convective impulse at its highest altitude of 14-15 km during legs 1 to 3, but then most of the cloud mass was detrained further below, presumably at the level of neutral

buoyancy. Either cloudy air, or the moist precursors to cloud, were detrained or formed at ~ 14 km altitude, where θ_e values were within ± 2 K of those measured within the convective impulse. We do not believe this cloud was advected over the storm anvil from another location; horizontal transects through the tropopause layer showed that it had nearly identical horizontal dimensions to the the anvil beneath it. Since this feature was observed above anvils on other days during CRYSTAL-FACE, we hereafter refer to this upper cloud layer as thin tropopause cirrus (TTC), while the thicker lower cloud is referred to as the anvil.

Figure 3

4. Microphysical and single-scattering properties

4.1. Vertical profile

Measurements of microphysical and radiative parameters obtained during the vertical profile of the TTC and anvil are shown in Figs. 4 and 5, respectively. At the time of the profile, the anvil was still attached to the convective core.

Figure 4

Shown size distributions are normalized by total concentration in order to clarify differences in the shape of the size distribution. Within the TTC the size distribution was mono-modal, and the particles measured did not usually exceed $100 \mu\text{m}$ maximum dimension (hereafter ice crystal sizes will be expressed in terms of maximum dimension unless otherwise stated) and the mode size in the number distribution was located at about $20 \mu\text{m}$. CPI images showed a few columns, spheres, and irregularly shaped ice crystals, with most of the columns and spheres found at the bottom of the TTC (Fig. 6).

Figure 5

For the majority of the profile, the relative humidity was well above ice saturation, reaching a maximum value of $\sim 150\%$ in the middle of the cloud, compared to $\sim 100\%$ in ambient clear

Figure 6

air. This is where ice crystals were smallest, which suggests that haze aerosols in the layer were actively freezing homogeneously to form new ice crystals. The TTC was very tenuous with total ice crystal concentrations usually below 500 L^{-1} and an average *IWC* of 0.00125 g m^{-3} . Through the depth of the profile, the vertically integrated ice water content, or ice water path (*IWP*), was $\sim 1.5 \text{ g m}^{-2}$.

Optical properties of the layer are shown in Fig. 5b. Values of β_{ext} in the TTC were consistently below the CIN lower detection threshold of 0.4 km^{-1} , so extinction, effective radius and visible optical depth are estimated from CAPS data, assuming spherical particles over the CAS size range. In thicker clouds measured during CRYSTAL-FACE, CIN measurements of β_{ext} were usually highly correlated but 30 to 40% higher than estimates from the CAPS probe, which is within experimental uncertainty (Garrett et al., 2003). CAPS cumulative optical depth τ for the cloud was 0.2 while values of β_{ext} were at or below 0.2 km^{-1} throughout the cloud's depth, with values for r_e of $\sim 10 \mu\text{m}$.

The anvil proper was an hour and a half old when it was profiled vertically by the Citation. Considering this particular storm was not particularly strong compared to others measured during CRYSTAL-FACE, maximum values of *IWC* in the profile were quite high, reaching 0.30 g m^{-3} over much of the profile. Above 9500 m altitude, size distributions had two modes, located at $\sim 30 \mu\text{m}$ and $\sim 105 \mu\text{m}$ maximum dimension. Below 9500 m altitude, the larger mode was absent. *In situ* and atmospheric sounding data (Fig. 2) showed that below this level winds also shifted, from 5 m s^{-1} northwesterly to 10 m s^{-1} northeasterly. It is unclear what the influence of different ice crystal trajectories might be on the size distribution. Assuming the smaller cloud mode was composed of solid ice spheres, it contributed approximately 20% to total *IWC* over the depth of the anvil.

Vertical fluctuations in IWC and N in Fig. 4b are probably seen because the Citation repeatedly flew across a horizontal gradient in cloud density with each successive turn in the spiral ascent. This variability aside, IWC and N are surprisingly uniform vertically. This contrasts with earlier measurements in low-latitude thunderstorm anvils, which have generally shown smaller values of IWC near cloud top (e.g., Heymsfield, 1986).

Fig. 5b), shows a profile of the measured cloud optical properties. The extinction coefficient was also relatively uniform with height, and highly correlated with IWC and N . Mean values of β_{ext} were approximately 10 km^{-1} . The cumulative visible optical depth τ and ice water path IWP for the layer derived from *in situ* measurements of β_{ext} and IWC was 21.7 and 240 g m^{-2} , respectively. Values of the asymmetry parameter g measured in the anvil were about 0.74, which is approximately what has been found theoretically for idealized fractal ice crystals (Macke, 1993) and has been measured within cirrus in the Arctic (Garrett et al., 2001).

The effective radius (Eq. 1) in the upper 1500 m of the anvil was approximately $18 \mu\text{m}$, gradually increasing from 9500 m altitude to $25 \mu\text{m}$ in the 1000 m below. The location of this transition corresponds roughly with the beginning of a $150 \mu\text{m}$ precipitation mode in the ice crystal size distribution (Fig. 4b). Below this level, this precipitation mode was absent, but very large ice crystals $> 1000 \mu\text{m}$ became increasingly prevalent. Apparently, these very large ice crystals contributed only to a rather modest increase in r_e of $\sim 50\%$ at cloud base. CPI images also showed these large crystals were primarily aggregates of plates that had undergone varying degrees of evaporation as they fell (Fig. 7). Small crystals $< 50 \mu\text{m}$ diameter, found mostly near cloud top, were quasi-spherical in shape. A few pristine hexagonal plates were also observed.

Figure 7

The relative humidity in the anvil was near or below ice saturation for the majority of the profile (Fig. 4b), compared to $\sim 60\%$ in ambient clear air. Since high supersaturations with

respect to ice are required for ice production due to homogeneous freezing of haze particles (Koop et al., 2000), homogeneous nucleation of any new ice crystals from haze particles had probably ceased at the level of flight measurement. In this case, the observed ice crystals were likely either ejected from the storm updraft or formed near the anvil base and lofted upwards.

4.2. Horizontal transects

During the period of strong convection, while the anvil was forming, the WB-57F sampled the storm cloud along a southeast-northwest trajectory across the anvil's downwind axis. Following anvil separation from the storm, flight legs were flown along the anvil's axis (Fig. 3). The Citation flew only along-axis transects, in coordination with the WB-57F. Combined, the transects from the two aircraft paint a picture of the evolution of cloud microstructures in the TTC and anvil.

4.2.1. Across axis

During legs 1 to 3 the WB-57F sampled cloud across-wind approximately 20 km downwind of the core of a thunderstorm convective impulse that reached maximum intensity at 1840 UTC, according to N-POL radar imagery. Ice crystal size distributions measured during these legs are shown in Fig. 8. Leg 1 was at 14.7 km altitude, followed by legs 2 and 3 in descending 600 m intervals.

The shapes of the number size distributions were similar in each case, with comparatively high concentrations of large crystals (Fig. 8). A single mode, located at $\sim 20 \mu\text{m}$, was found at each altitude, and the slope of the size distribution was ~ 3 for ice crystals smaller than $200 \mu\text{m}$ and less than 1 for ice crystals larger than $200 \mu\text{m}$ (Fig. 8). That a few large ice crystals were present suggests the TTC cannot have formed entirely from *in situ* homogeneous nucleation, but

Figure 8

rather at least some portion must have come from the deep convection.

The bulk of the storm's second convective impulse at 1840 UTC was not sufficiently strong to reach 14.7 km altitude. Average N , IWC and β_{ext} at 14.7 km altitude were about 20 times lower than those measured just 15 min later at 14.1 km altitude (Table 1). Average N , IWC , and β_{ext} at 14.1 km were 10.7 cm^{-3} , 0.035 g m^{-3} and 9.0 km^{-1} , respectively, which is remarkably high considering measurements were made just a few hundred meters below the tropopause. Cloudy air at 1930 UTC and 13.5 km altitude (leg 3) was again very tenuous. Thus, it is possible the thick cloud measured during leg 2 spread to become the tenuous TTC layer.

Table 1.

4.2.2. Along axis

The TTC had a single mode in the ice crystal size distribution, located at $\sim 20 \mu\text{m}$, independent of altitude, cloud age or distance from the cloud's upwind edge, and few crystals larger than $200 \mu\text{m}$ (Fig. 8). Further there were no discernible spatial trends in IWC , N and β_{ext} . The average altitude, age, temperature, N , IWC , β_{ext} , r_e and RH at 14.1 km altitude (legs 5 and 9) and 13.5 km altitude (legs 6 and 8) are listed in Table 1. Average age represents the approximate flight leg-averaged age of the cloud mass, relative to its time of initial detrainment from the convective updraft, as determined from satellite imagery. At 14.1 km, average N decreased by 78% over 50 minutes of evolution, while at 13.5 km N increased by 210% over 25 minutes of evolution. The effective radius and relative humidity showed no dependence on either altitude or age but the temperature at each altitude warmed by 1°C . Thus, rather than dissipating, the cloud appears to have been slowly subsiding. The relative humidity within the TTC consistently remained above ice saturation during its evolution. Plausibly the effective radius remained at about $6 \mu\text{m}$ (Table 1), despite the supersaturated conditions, due to a close balance between

Maxwellian growth of small crystals and sedimentation of large crystals.

In contrast to the TTC, the anvil was characterized by a distinct bi-modal ice crystal size distribution (Fig. 9). The cloud mode was centered at about $25 \mu\text{m}$ and changed neither with distance downwind from the anvil leading edge nor anvil age. At approximately one hour age (leg 3), the precipitation mode, centered near $150 \mu\text{m}$ at the upwind edge of the anvil, increased in size over an approximate 30 km distance downwind to $700 \mu\text{m}$ at the anvil's downwind edge. This size shift with distance was not as evident at the same altitude 60 minutes later (leg 5), but rather remained at a constant mode size of about $150 \mu\text{m}$.

Figure 9

Averaged over all Citation legs 1 to 6, IWC , N , RH , β_{ext} and r_e were highest at the upwind edge of the anvil, and decreased as distance increased downwind (Fig. 10). The relative humidity became progressively subsaturated downwind from the anvils leading edge, decreasing from 95% to $\sim 60\%$ over a distance of 35 km. Measurements of g had a high level of uncertainty, since the extinction was relatively low. However, values remained approximately uniform over the length of the anvil.

Figure 10

At an altitude of 11.2 km (legs 1 and 6), which was near the top of the anvil, N , IWC and β_{ext} fell by about 90% over a period of about one and a half hours (Table 2). At an altitude of 10.6 km (legs 3 and 5), r_e stayed constant at about $17 \mu\text{m}$, while N , IWC , and β_{ext} fell by about a factor of three over a period of about 60 minutes. The relative humidity at each altitude simultaneously decreased by about 10% in each interval, while the temperature remained constant. The total water content (vapor and ice) TWC , which would be a conserved variable in the absence of mixing or precipitation, fell by 50% between legs 1 and 6, and 30% between legs 3 and 5.

Table 2.

5. Radiative fluxes

5.1. Radiative Forcing

We examine the effect of the observed evolution of the anvil microphysical properties on net cloud radiative forcing at the top of the troposphere (TOT CRF_{net}) using GOES-8 satellite imagery, radiometer measurements from the WB-57F during leg 3, and *in situ* data obtained from the Citation from leg 5. For these two legs the WB-57F and Citation were vertically stacked and close in time and horizontal space. CRF_{net} is defined here as the difference between cloudy and clear sky measurements of the sum of the net longwave and shortwave radiative fluxes, assuming 100% cloud cover. Thus negative (positive) values at the TOT represent a tropospheric cooling (warming) by a cloud.

Radiometer measurements of shortwave and longwave broadband radiative fluxes from leg 5 of the WB-57 were used to calculate TOT CRF_{net} . This is an imperfect measure because the WB-57F was actually within the TTC cloud layer, rather than above all cloud. However, during leg 5 the WB-57 was at 14.1 km altitude, in the uppermost part of an already thin TTC layer. Thus any contribution to TOT CRF_{net} from higher cloud was probably negligible.

Secondly, although we focus here on radiative forcing by the anvil, the TTC contributes to TOT forcing itself. The magnitude of this effect is addressed later.

Clear sky fluxes used for calculations of CRF_{net} were obtained from airborne radiative flux measurements in clear sky. Clear sky periods were determined from GOES-8 retrievals of IWP for pixels that corresponded to the aircraft flight track.

The trends in radiative forcing downwind along the length of the anvil were estimated by taking *in situ* measurements of IWC and r_e from within the anvil and TTC as inputs to the

Streamer radiative transfer model (Key, 2001). Although Streamer has a more limited infrared wavelength resolution than many other band models that focus on gases, it allows the user to explicitly define multiple cloud layers with unique values of effective radius, ice water content, and ice crystal habit. A phase function representative of idealized “rough aggregates” ice crystals was assumed here (Yang and Liou, 1998) because it corresponds to values of the asymmetry parameter similar to those actually measured in the anvil.

Instantaneous radiative fluxes were calculated for the time and date of the flight legs using the Streamer discrete ordinates solver. Here, we adopted four streams for shortwave and two streams for infrared calculations. Atmospheric profiles were based on those shown in Fig. 2. The anvil cloud top and vertical dimensions, and the IWC and r_e of the TTC were defined in the model consistent with the measurements shown in Fig. 4 and Fig. 5.

For these specifications, TOT CRF_{net} for the anvil-TTC system was then calculated for a wide range of values of anvil IWP and r_e . Superimposed on the resulting contour plot (Fig. 11), the trend in CRF_{net} along the length of the anvil is determined in two ways.

In the first approach, CRF_{net} is found from Fig. 11 based on *in situ* trends in anvil r_e and anvil IWC measured aboard the Citation during leg 3. To obtain CRF_{net} requires assuming a value for cloud thickness in order to convert measured IWC to IWP . To do this we take GOES-8 retrievals of IWP from where the Citation was at the anvil’s upwind edge and compare this to the *in situ* measurement of IWC . Since the satellite IWP was approximately 100 g m^{-2} , and the aircraft measured IWC was about 0.2 g m^{-3} , we infer that the cloud thickness Δz during Citation leg3 was 500 m. Thus, the anvil had thinned rapidly since the airborne profile an hour earlier 4 when Δz was 2.5 km and the anvil was still attached to the convection.

We have confidence that this estimate of Δz is fairly accurate for two reasons. Firstly, at

the time of the airborne vertical profile, both GOES-8 retrievals and vertically integrated *in situ* measurements of IWP showed the anvil IWP was $\sim 250 \text{ g m}^{-2}$. (During the profile, satellite retrieved IWP was derived from an average over a box enclosing the spiral flight path during a series of three GOES-8 images during the time period of the spiral. This method was chosen because aircraft measurements are continuous within an evolving cloud, while satellite images are snap shots taken every 10 minutes). Secondly, in practice retrievals of IWP are inferred from retrievals of τ and r_e . Although we cannot validate τ for flight transects, Fig. 10 shows *in situ* and retrieved r_e were in closest agreement at the upwind edge of the anvil cirrus.

In the second approach for deriving trends in CRF_{net} (Fig. 11), Citation measurements of anvil r_e were combined with nearly simultaneous WB-57F measurements of CRF_{net} from above the anvil-TTC system. For the calculations, the TTC was assumed to have a fixed visible optical depth of 0.3, and an effective radius of $9 \mu\text{m}$.

Comparison of these two approaches does not represent a closure study between modeled and measured fluxes. In fact, the WB-57F and Citation aircraft were horizontally separated by about 15 km. Second, both approaches employ *in situ* measurements of r_e . However, the comparison is useful for corroborating *trends* in net forcing by the TTC-anvil system as it evolves.

The two approaches show close agreement. They show a trend towards less tropospheric cooling along the downwind length of the anvil-TTC system. Precipitation depletes IWP , while simultaneously decreasing r_e . The reduction in r_e slows the warming trend, but it is the trend in IWP that dominates CRF_{net} .

Although, Fig. 11 focuses on TOT CRF_{net} by the anvil, it would be interesting to estimate the effect the presence of the TTC on the calculations, particularly considering a multi-layered structure is not typically assumed in calculations of the radiative effects of anvil cirrus.

Figure 1

To estimate this effect, we ran the above calculations with the TTC removed from the atmospheric profile, and then subtracted the resulting TOT CRF_{net} from the results shown in Fig. 11. Values of r_e and IWP obtained from measurements in the anvil are superimposed on the calculated difference (Fig. 12).

The results show that the TTC had no impact on TOT radiative forcing by the anvil when it was thick. However, once the anvil IWP had thinned to 10 g m^{-2} , at which point it was no longer a blackbody, the TTC contributed -7 W m^{-2} to total forcing by the anvil-TTC system, which is about 10% of the total.

In an assumed absence of an anvil beneath the TTC, calculated radiative forcing by the TTC alone at 2024 UTC would have been -15 W m^{-2} .

Figure 1

5.2. Radiative heating

Since the TTC had a visible optical depth of just ~ 0.3 (Fig. 5), in an otherwise cloudless sky it would be strongly heated from below. Such heating would be expected to either loft the cloud layer or rapidly dissipate the cloud (Jensen et al., 1996). This was not observed. Rather, the TTC settled and was microphysically very stable. Here we explore a proposal by Hartmann et al. (2001), that the presence of a thick anvil below the TTC might lead it to cool. Effectively, graybody TTC equilibrates not to the Earth's surface but to the anvil, which is much colder.

For the case presented here, the TTC was directly situated above the anvil, and had similar horizontal dimensions (Garrett et al., 2004). Based on the radiative transfer calculations presented above, in the absence of the anvil, estimated heating rates \mathcal{H} in the TTC would have been 5 K/day. In it's presence, calculated heating rate profiles are shown in Fig 13. For a thick anvil still attached to the convective core (e.g. $\Delta z = 2.5 \text{ km}$, $\tau = 21$ and $r_e = 20 \text{ }\mu\text{m}$), the calculated TTC cooling

rate is about 0.2 K/day. For a thin detached anvil, with $\Delta z = 0.5$ km, $\tau = 2$ with $r_e = 12$ μm , the TTC heated by about 1 K/day. For a similar cloud scenario observed over the Tropical Western Pacific, Comstock et al. (2002) calculated heating rates in the TTC of 0.53 K/day, mostly due to IR heating.

Figure 1

If, for the sake of argument, no anvil was present below the TTC, the heating rate would have been about 7 K/day. Therefore, as suggested by Hartmann et al., it appears that the TTC lifetime was prolonged by the anvil's presence. Unfortunately, no measurements were made of the TTC once the anvil had fully dissipated. However, Comstock et al.'s observations of tropical TTC showed that, even once a cirrus anvil has dissipated, TTC layers might persist for several days. Comstock et al. suggested that some other unknown mechanism must protect the cloud from evaporation, even when it is not shielded by an anvil beneath.

The anvil is principally characterized by concentrated heating at the anvil base and cooling at the anvil top (Fig. 13). While the anvil is strongly heated by terrestrial radiation from below, it radiates strongly through its top to outer space. Smaller heating rates in the anvil interior are due to solar heating. As the anvil evolves, its base rises and it becomes less opaque to thermal radiation. The anvil top is then no longer shielded by the anvil interior from terrestrial heating. The anvil heating profile then becomes progressively asymmetric, with more pronounced heating at the bottom than the top of the anvil. At the anvil base, peak \mathcal{H} increases from about 125 K/day when the anvil is thick and attached to the convective core, to 150 K/day when it is thinner and detached from the convective core. Simultaneously, at cloud top, peak cooling decreases from 100 K/day to 25 K/day.

The vertical distribution of heating is less uniform than described in Ackerman et al.'s (1988) description of heating rates in tropical anvils because a) the anvil top is about 25 °C warmer than

the tropopause, and b) the ice crystals have smaller effective radii, making them more efficient absorbers of infrared radiation. The implications of these profiles for the anvil's dynamic evolution are discussed in Section 6.3.

6. Discussion

6.1. Small ice crystals

The anvil and TTC shown in this study had high concentrations of small non-precipitating ice crystals. Although similarly small crystals have been sampled in anvil and mid-latitude cirrus elsewhere (e.g. Heymsfield and McFarquhar, 1996, Ström et al., 1997) and were observed in all other anvil and TTC clouds sampled during CRYSTAL-FACE (Garrett et al., 2003), their presence in high concentrations remains contentious; it is often argued that the probes usually used to measure these ice crystals artificially inflate the concentrations of small ice crystals due to shattering on the instrument inlet (Gardiner and Hallet, 1985; Gayet et al., 1996).

On the other hand, bulk cloud probes measuring cloud mass and optical extinction during CRYSTAL-FACE should be insensitive to ice crystal breakup. IWC remains conserved under crystal disintegration. Extinction would be inflated by breakup, but the CIN probe used to measure optical extinction has no inlet but rather a broad and aerodynamic aperture relative to both the width of the measurement laser beam and the sizes of large ice crystals.

For each flight leg within the anvil, the effective diameter D_e (twice the effective radius), derived with bulk cloud probe data from Eq. (1), decreased from approximately $45\ \mu\text{m}$ near the upwind edge of the anvil to approximately $25\ \mu\text{m}$ near the anvil's downwind edge. Within the TTC, measured D_e was approximately $10\ \mu\text{m}$ to $20\ \mu\text{m}$ independent of cloud age or distance

downwind.

These calculated values of D_e correspond well with the location of the cloud mode in the measured ice crystal size distributions, especially in the downwind region of the anvil where precipitation ice crystals were largest, but in the lowest concentrations. Because large irregular ice crystals were observed in the anvil, and to a lesser extent in the TTC, inflated concentrations of small particles due to ice crystal shattering cannot be ruled out. However, the consistency between bulk and size distribution measurements suggests this effect was probably small.

In addition, N and β_{ext} for all Citation legs were highly linearly correlated with a slope of 227 km l^{-1} (Fig. 14). In general, β_{ext} and N are related by

$$\beta_{ext} \simeq \frac{\pi}{2} N \bar{D}^2 \quad (2)$$

From the data shown in Fig. 14, $\bar{D} \simeq 37 \text{ } \mu\text{m}$, which is in between the values of D_e measured at the upwind and downwind edges of the anvil (Fig. 10). Thus, in contrast to the findings of Heymsfield et al. (1996), small ice crystals appear to have made an important contribution the anvil radiative properties.

Figure 1

6.2. Microphysical evolution

A full understanding of the evolution of a cirrus anvil requires a detailed model with coupled dynamics, radiation and microphysics. Here we describe the mechanisms controlling the evolution of the 21 July anvil based on an interpretation of the previously described observations and calculations.

The anvil became progressively subsaturated with distance downwind from its upwind edge

(Fig. 10). It has been argued that most anvil ice crystals form from homogeneous freezing of haze particles entrained into convective updraft cores (Fridlind et al., 2004). Once ejected from the convection, their exposure to subsaturated conditions in the anvil might be expected to result in a shift of the measured cloud mode to smaller sizes as the anvil evolved. For example, given the humidity conditions observed during Citation leg 5 (Table 2), the time scale for a $20\text{ }\mu\text{m}$ crystal to sublimate to $10\text{ }\mu\text{m}$ is about one minute. However, anvil ice crystal size distributions (Fig. 9) show no correspondence between the age of the air parcel and the size of the cloud mode ice crystals.

This is surprising, and it is unclear how the small mode of the size distribution can be maintained under subsaturated conditions. Possible explanations include: 1. Large crystals were in fact breaking up in the FSSP-100 inlet, which may have masked any such shift. However, as discussed in Sec. 6.1, it seems unlikely from bulk probe data that such breakup was in fact significantly affecting measured size distributions. 2. As aggregate ice crystals evaporate, they may break-up to maintain a small particle mode (Bacon et al., 1998). 3. Small crystals might be replenished by small scale updrafts carrying crystals from subsaturated regions below the Citation flight level (Zender and Kiehl, 1994). This can occur if large ice crystals below cloud base shrink due to evaporation, and then are subsequently lofted back into the anvil. 4. It may be that complete evaporation is occurring, but in subsaturated pockets smaller than the spatial resolution of the aircraft measurements. In such case, measured RH , N and IWC might decrease as the anvil evolves, but without any apparent shrinkage of ice crystals. 5. Ice crystals are regenerated at the anvil base from haze particles and subsequently lofted upward by internal circulations in the anvil.

Large aggregates increased in size and concentration between the upwind and downwind edges of the anvil (the precipitation mode in Fig. 9a)). This shift in the precipitation mode with distance downwind from the anvil's upwind edge disappeared by the time the anvil aged

an additional hour (Fig. 9b). What appears to have occurred is that, in the 40 minutes evolution that separated the downwind from the upwind edge of the anvil, ice crystals ejected from the convective core aggregated further in the anvil, increasing in size by a factor of ~ 4 while decreasing in concentration by a factor of ~ 10 . Large aggregates settled quickly, at a rate of $\sim 1 \text{ m s}^{-1}$ (Heymsfield et al., 2002), and although internal circulations in the anvil may have slowed their descent, they were removed rapidly from the anvil plume as precipitation, further aggregating on their way to cloud base. The very largest aggregates ($>1000 \text{ }\mu\text{m}$ across) were only observed at the very lowest levels of the anvil and at the earliest stages of anvil detrainment (Fig. 4b).

Over the course of about an hour, TWC in the anvil fell by $\sim 0.06 \text{ g m}^{-3}$ (Table 2). Assuming mass and fall speed relationships for the measured size distributions of precipitating ice crystals that are suitable for aggregates of side-planes (Heymsfield et al., 2002), and an anvil thickness of 1 km, the approximate loss rate of TWC and IWC due to precipitation was $0.05 \text{ g m}^{-3} \text{ h}^{-1}$. Therefore, in addition to evaporative losses, the anvil is dessicated by the settling of ice crystal aggregates.

6.3. Dynamical evolution

Thermodynamically, the temperature of the anvil stayed nearly constant over the course of an hour (Table 2). Despite strong calculated radiative heating gradients, the anvil stayed stably stratified over two hours evolution. Based on the measured differences in θ between 10.6 and 11.2 km altitude (Table 2), the anvil stratification $d\theta/dz$ was about 2.2 K km^{-1} . Similar stratification was measured during the initial profile of the anvil and also in environmental air (Fig. 2).

Based on the *in situ* meteorological data obtained during the Citation profile of the anvil, the bulk Richardson number Ri for the entire anvil layer was approximately 5. At about three quarters

hour and two hours age, Ri was about 3 and 1, respectively (Table 2). These values are larger than the critical value ($Ri_{crit} = 0.25$) below which it is usually assumed that turbulence is sustained. Unfortunately, due to sporadic performance of the gust probe no vertical profile was obtained of the buoyancy flux in the anvil. However, no vigorous updrafts were measured. The standard deviation of the updraft velocity measured by the Citation at 10.6 km altitude (legs 3 and 5) was 0.25 m s^{-1} .

Discussions of the dynamical evolution of anvil layers (Ackerman, 1988; Lilly, 1988) often assume that net heating of the layer drives the cloud as a whole vertically upwards through the stratified tropopause transition layer. If the anvil precipitates as it is lofted into the lower stratosphere, it plausibly accounts for observations of lower than expected humidities there (Danielsen, 1982). These studies also typically assume that differential heating, with a heating rate that decreases upwards, drives convection and so maintains an adiabatic lapse rate within the cloud.

The measurements presented here show, firstly, that the anvil did not heat significantly over the course of about two hours so that no rise of the cloud as a whole is expected. Secondly, the stratification of the cloud stayed nearly identical to that of its environment and the Richardson number for the layer was high.

Thus, it seems worth considering whether, instead of driving turbulent mixing throughout the entire depth of the layer, cooling at cloud top and heating at cloud base drive horizontal motion instead, and maintain the vertical stratification.

Consider Fig. 13, where the anvil interior is radiatively shielded by strongly absorbing/emitting layers at the anvil base and top. One possible scenario involves assuming potential temperature surfaces stay flat. Then, in the absence of horizontal temperature gradients or heating

in the anvil, the vertical velocity component for the radiatively interacting layers is given simply by $w_{strat} = \mathcal{H} / (d\theta/dz)$. The top of the cloud sinks and the bottom rises in response to the heating. The cirrus just thins and spreads. The rate of spreading of the radiative layer away from the horizontal center of the anvil cirrus is given by the continuity equation, and by scale analysis should be of order $u_{strat} \sim Lw_{strat}/h$, where L is the half-width of the anvil and h is the penetration depth of infrared radiation into the cirrus. Note that h does not change greatly as the anvil evolves because at the same time the cloud loses mass, r_e gets smaller and the existing mass absorbs/emits thermal radiation more effectively.

In the above scenario, spreading of the anvil involves associated inertial accelerations that require horizontal pressure gradients. The spreading velocity u_{strat} is then the speed required for no major disruption to surfaces of constant potential temperature.

A second scenario is that strong radiative heating or cooling in the radiative layer may cause a depth h at the cloud top and bottom to become well-mixed, while the cirrus interior stays stratified. In this case, horizontal gradients in θ are produced, and these cause the mixed-layer to spread laterally at a rate $u_{mix} \sim Nh$ (Scorer, 1978), where N is the buoyancy frequency of the environment.

For the first scenario to be most important, u_{strat} would have to be less than u_{mix} ; e.g. any pressure perturbation due to heating would preferentially drive stratified ascent rather than mixing. Assuming characteristic values for N ($\sim 0.01 \text{ s}^{-1}$), w_{strat} (0.1 m s^{-1}), L ($\sim 10 \text{ km}$) and h ($\sim 100 \text{ m}$), estimated spreading rates according to these two mechanisms are $u_{strat} \sim 10 \text{ m s}^{-1}$ and $u_{mix} \sim 1 \text{ m s}^{-1}$. Since $u_{mix} \ll u_{strat}$, it appears most likely that the reason the anvil spreads is because concentrated radiative heating creates fronts of depth h , composed of well-mixed cold and warm air, that push laterally into their environment.

The above estimate for u_{mix} is approximately consistent with satellite imagery, which shows that the anvil spread to either side of its center at a rate of $\sim 2 \text{ m s}^{-1}$ between 1945 and 2045 UTC (Fig. 1c and d). However, this frontal mechanism for spreading might be inconsistent with observations showing maintenance of vertical stratification in the anvil. A possible explanation for this discrepancy is that, in fact, it was only the very top and bottom of the anvil were well-mixed, but that this escaped notice because perhaps the aircraft did not adequately profile these portions of the cloud. We intend to explore this issue further by investigating temperature profiles of spreading anvil cirrus measured on other days during CRYSTAL-FACE.

7. Conclusions

We have presented here *in situ* measurements of cloud microphysical and single-scattering properties within an evolving cirrus anvil observed west of south Florida on 21 July 2002. The anvil detrained from a relatively weak storm that developed along a sea breeze front, and was isolated from other convective cells. The anvil was well characterized by two aircraft over a period of 3 hours, which made it an ideal candidate for case study. While the convective core of the storm moved eastward, the anvil developed in northeasterly flow and spread over the Gulf of Mexico. From this study we have come to the following conclusions.

1. As with many other anvils observed during CRYSTAL-FACE (Garrett et al., 2004), the anvil had two distinct layers. Separated vertically from an optically thick anvil layer by 1.5 km was a second cloud layer distributed equally between the upper troposphere and lower tropopause. This second layer was termed thin tropopause cirrus (TTC). Although 1.5 km thick, it was extremely tenuous with IWC values of about 1 mg m^{-3} and a visible

optical depth of just ~ 0.3 . The size distribution was characterized by a single mode of small ice crystals with an effective radius of 4 to 10 μm . The microphysical properties of the TTC were quasi-steady over the sampling period. This might be because, as pointed out by Hartmann (2001) and confirmed in radiative transfer calculations presented here, a lower anvil layer can shield the TTC from the intense flux of infrared radiation from the surface. If the anvil is thick, the TTC cools. Garrett et al. (2004) hypothesized that TTC originate as convectively forced pileus clouds, spreading as buoyancy waves near the tropopause. Plausibly, over low-latitudes these TTC might be common and evolve to become the widespread subvisible cirrus apparently centered around tropical convection (Pfister et al. 2001; Dessler and Yang, 2003).

2. In the anvil layer itself, the ice crystal size distribution was bi-modal. In its early stages, it was characterized by a cloud mode centered at 30 μm maximum dimension and a precipitation mode composed of aggregate ice crystals. The location of this mode was centered at about 150 μm maximum dimension at the anvil's leading edge, and at the anvil's trailing edge 30 km downwind, this mode shifted to 700 μm maximum dimension. At the same altitude, almost an hour later, this size shift was no longer observed because the largest ice crystals had precipitated.
3. Concentrations of crystals in the cloud mode were up to one thousand times higher than in the precipitation mode. These small crystals dominated the anvil radiative properties, particularly at the downwind edge of the anvil where large ice crystals had precipitated. Ice crystal effective radii r_e decreased from 20 μm to 12 μm as the anvil evolved.
4. In two hours from when the anvil detached from the convective core, the anvil IWC fell

from 0.3 g m^{-3} to 0.01 g m^{-3} . This was primarily due to precipitation but evaporation may have also played an important role. At the same time the cloud thinned from a depth of about 2.5 km to 0.5 km.

5. The instantaneous net top-of-troposphere radiative forcing was strongly cooling at the anvil leading edge, but tended towards zero as the anvil thinned downwind. While the decrease in IWP dominated this trend, it was slowed by the simultaneous decrease in r_e . The TTC made a negligible contribution to the overall forcing by the cloud system except when the anvil became highly transparent.
6. Because small ice crystals dominated the anvil radiative properties, absorption/emission of radiation by the anvil cirrus was concentrated in the top and bottom 100 m of the cloud, while the interior was largely shielded from rapid heating. Like its environment, the cloud maintained a stratification of about 2 K km^{-1} . This was in spite of the rapid cooling (heating) at cloud top (bottom), which might normally be assumed to make the anvil cirrus well mixed. We argue that, rather than driving convection through the entire layer, the concentrated interaction with thermal radiation at the cloud vertical boundaries creates thin frontal tongues that spread the anvil cirrus laterally, leaving the interior comparatively unperturbed.

Acknowledgments. This work was supported by the NASA CRYSTAL-FACE project. We appreciate stimulating discussions with S. Krueger and C. Garrett about anvil cirrus dynamics, a helpful review from D. Wilson, and efforts of the flight crews of the NASA WB-57F and University of North Dakota Citation during CRYSTAL-FACE

References

- Ackerman, T. P., K.-N. Liou, F. P. J. Valero, and L. Pfister, 1988: Heating rates in tropical anvils. *J. Atmos. Sci.*, **45**, 1606-1623.
- Bacon, N. J., B. D. Swanson, M. B. Baker, and E. J. Davis, 1998: The breakup of levitated frost particles, *J. Geophys. Res.*, **103**, 13763-13775.
- Baumgardner, D., H. Jonsson, W. Dawson, D. O'Connor and R. Newton, 2002: The cloud, aerosol and precipitation spectrometer (CAPS): A new instrument for cloud investigations, *Atmos. Res.*, **59-60**, 251-264.
- Buck, A., 1985: The lyman-alpha hygrometer. *Moisture and Humidity: Measurement and Control in Science and Industry*, Proc. 1985 Int. Symp. on Moisture and Humidity, Washington, DC, Instrument Society of America, 411-436.
- Comstock, J. M, T. P. Ackerman, and G. G. Mace, 2002: Ground-based lidar and radar remote sensing of tropical cirrus clouds at Nauru Island: Cloud statistics and radiative impacts. *J. Geophys. Res.*, **107**, 4714, doi:10.1029/2002JD002203.
- Danielson, E. F., 1982: A dehydration mechanism for the stratosphere. *Geophys. Res. Lett.*, **9**, 605-608.
- Dessler, A. E., and P. Yang, 2003: The distribution of tropical thin cirrus clouds inferred from Terra MODIS data. *J. Climate*, **16**, 1241-1247.
- Foot, J. S, 1988: Some observations of the optical properties of clouds, Part 2, Cirrus. *Q. J. R. Meteorol. Soc.*, **114**, 145-164.
- Fridlind, A. M., A. S. Ackerman, E. J. Jensen, A. J. Heymsfield, M. R. Poellot, D. E. Stevens, D. Wang, L. M. Miloshevich, D. Baumgardner, R. P. Lawson, J. C. Wilson, R. C. Flagan, J. H. Seinfeld, H. H. Jonsson, T. M. VanReken, V. Varutbangkul, and T. A. Rissman, 2004: Evidence for the predominance of mid-tropospheric aerosols as subtropical anvil cloud nuclei. *Science*, **304**, 718-722, doi: 10.1126/science.1094947
- Gardiner, B. A., and J. Hallett, 1985: Degradation of in-cloud forward scattering spectrometer probe measurements in the presence of ice particles. *J. Atmos. Oceanic Tech.*, **2**, 171-180.

Garrett, T. J., P. V. Hobbs, and H. Gerber, 2001: Shortwave, single-scattering properties of arctic ice clouds *J. Geophys. Res.* **106**, 15155-15172.

Garrett, T. J., H. Gerber, E. M. Weinstock, C. H. Twohy, and D. G. Baumgardner, 2003: Small, highly reflective ice crystals in low-latitude cirrus. *Geophys. Res. Lett.*, **30**, 2132, doi:10.1029/2003GL018153.

Garrett, T. J., A. J. Heymsfield, M. J. McGill, B. A. Ridley, D. G. Baumgardner, P. T. Bui, C. R. Webster, 2004: Convective generation of cirrus near the tropopause. *J. Geophys. Res.*, (in press).

Gayet, J-F, G. Febvre, and H. Larsen, 1996: The reliability of the PMS FSSP in the presence of small ice crystals. *J. Atmos. Oceanic Tech.*, **13**, 1300-1310.

Gerber, H., Y. Takano, T. J. Garrett, and P. V. Hobbs, 2000: Nephelometer measurements of the asymmetry parameter, volume extinction coefficient, and backscatter ratio in Arctic clouds. *J. Atmos. Sci.*, **57**, 3021-3034.

Griffith, K. T., S. K. Cox, and R. G. Knollenberg, 1980: Infrared radiative properties of tropical cirrus clouds inferred from aircraft measurements. *J. Atmos. Sci.*, **37**, 1077-1087.

Hartmann, D. L., J. R. Holton, and Q. Fu, 2001: The heat balance of the tropical tropopause, cirrus, and stratospheric dehydration, *Geophys. Res. Lett.*, **28(10)**, 1969-1972, 10.1029/2000GL012833.

Heymsfield, A. J., 1986: Ice particle evolution in the anvil of a severe thunderstorm during CCOPE. *J. Atmos. Sci.*, **43**, 2463-2478.

Heymsfield, A. J., and G. M. McFarquhar, 1996: High albedos of cirrus in the tropical Pacific warm pool: Microphysical interpretations from CEPEX and from Kwajalein, Marshall Islands. *J. Atmos. Sci.*, **53**, 2424-2451.

Heymsfield, A. J., G. M. McFarquhar, W. D. Collins, J. A. Goldstein, F. P. J. Valero, W. Hart, and P. Pilewskie, 1998: Cloud properties leading to highly reflective tropical cirrus: Interpretations from CEPEX, TOGA COARE, and Kwajalein, Marshall Islands. *J. Geophys. Res.*, **103**, 8805-8812.

Heymsfield, A. J., S. Lewis, A. Bansemer, J. Iaquinta, L. M. Miloshevich, M. Kajikawa, C. Twohy, and M. Poellot, 2002: A general approach for deriving the properties of cirrus and stratiform ice cloud particles. *J. Atmos. Sci.*, **59**, 3-29.

Iacobellis and Somerville, 2000: Implications of microphysics for cloud-radiation parameterizations: Lessons from TOGA COARE. *J. Atmos. Sci.*, **57**, 161-183.

Jensen, E. J., O. B. Toon, H. B. Selkirk, J. D. Spinhirne, and M. R. Schoeberl, 1996: On the formation and persistence of subvisible cirrus clouds near the tropical tropopause. *J. Geophys. Res.*, **101**(16), 21361-21375.

Khelif, D. S., S. P. Burns, and C. A. Friehe, 1999: Improved wind measurements on research aircraft. *J. Atmos. Oceanic Tech.*, **16**, 860-875.

Knollenberg, R.G., A. J. Daschler, and D. Huffman, 1982: Measurements of the aerosol and ice crystal populations in tropical stratospheric cumulonimbus anvils. *Geophys. Res. Lett.*, **9**, 613-616.

Knollenberg, R. G., K. Kelley, and J. C. Wilson, 1993: Measurements of high number densities of ice crystals in the tops of tropical cumulonimbus. *J. Geo. Res.*, **98**, 8639-8664.

Koop, T, B. Luo, A. Tsias, and B. Peter, 2000: Water activity as the determinant for homogeneous ice nucleation in aqueous solutions. *Nature*, **406**, 611-614.

Lawson, R.P., B.A. Baker, C.G. Schmitt and T.L. Jensen, 2001: An overview of microphysical properties of Arctic clouds observed in May and July during FIRE.ACE. *J. Geophys. Res.*, **106**, 14989-15014.

Li, Y., 2003: Intensity of convective storms in Florida and their environmental properties. M.S. thesis, Dept. of Meteorology, University of Utah, 116 pp.

Lilly, D. K., 1988: Cirrus outflow dynamics. *J. Atmos. Sci.*, **45**, 1594-1605.

Macke, A., 1993: Scattering of light by polyhedral ice crystals. *Appl. Opt.*, **32**, 2780-2788.

May, R. D., 1998: Open-path, near-infrared tunable diode laser spectrometer for atmospheric measurements of H₂O. *J. Geo. Res.*, **103**, 19161-19172.

McFarquhar, G. M., and A. J. Heymsfield, 1997: Parameterization of tropical cirrus ice crystal size distributions and implications for radiative transfer: results from CEPEX. *J. Atmos. Sci.*, **54**, 2187-2200.

Minnis, P., and Coauthors, 1995: Cloud optical property retrieval (Subsystem 4.3). “Clouds and the Earth’s Radiant Energy System (CERES) Algorithm Theoretical Basis Document, Volume III: Cloud Analyses and Radiance Inversions (Subsystem 4)”, NASA RP 1376 Vol. 3, edited by CERES Science Team, pp. 135-176.

Minnis, P., D. P. Garber, D. Young, R. F. Arduini, and Y. Takano, 1998: Parameterizations for reflectance and emittance for satellite remote sensing of cloud properties. *J. Atmos. Sci.*, **55**, 3313-3339.

Noone, K.J., J. A. Ogren, J. Heintzenberg, R. J. Charlson, and D.S. Covert, 1988: Design and calibration of a counterflow virtual impactor for sampling of atmospheric fog and cloud droplets, *Aer. Sci. Technol.*, **8**, 235-244.

Ou, S. C., K. N. Liou, W. M. Gooch, and Y. Takano, 1993: Remote sensing of cirrus cloud parameters using Advanced Very High Resolution Radiometer 3.7 and 10.9 μm channels. *Appl. Opt.*, **32**, 2171-2180.

Payne, G. A., C. A. Friehe, and D. K. Edwards, 1994: Time and frequency response of a resistance-wire aircraft atmospheric temperature sensor. *J. Atmos. Oceanic. Tech.*, **11**, 463-475.

Pfister, L., H. B. Selkirk, E. J. Jensen, M. R. Shoeberl, O. B. Toon, E. V. Browell, W. B. Grant, B. Gary, M. J. Mahoney, T. V. Bui. and E. Hints, 2001: Aircraft observations of thin cirrus clouds near the tropical tropopause, *J. Geophys. Res.*, **106**, 9765-9786.

Scorer, R. S.: *Environmental Aerodynamics*, Ellis Horwood, 1978, pp. 488.

Scott, S. G., T. Paul Bui, K. Roland Chan, and W. Stuart, 1990: The Meteorological Measurement System on the NASA ER-2 aircraft. *J. Atmos. Oceanic Tech.*, **7**, 525-540.

Strom, J., B. Strauss, T. Anderson, F. Schroder, J. Heintzenberg, and P. Wendling, 1997: In situ observations of the microphysical properties of young cirrus clouds. *J. Atmos. Sci.*, **54**, 2542-2553.

Twohy, C. H., A. J. Schanst, and W. A. Cooper, 1997: Measurement of condensed water content in liquid and ice clouds using an airborne counterflow virtual impactor. *J. Atmos. Ocean. Tech.*, **14**, 197-202.

Weinstock, E. M., and Coauthors, 1994: New fast response photofragment fluorescence hygrometer for use on the NASA ER-2 and the Perseus remotely piloted aircraft. *Rev. Sci. Instrum.*, **65**, 3544-3554.

Valero, F.P.J., A. Bucholtz, B.C. Bush, S.K. Pope, W.D. Collins, and P. Flatau, 1997: Atmospheric Radiation Measurements Enhanced Shortwave Experiment (ARESE): Experimental and data details. *J. Geophys. Res.*, **102 (D25)**, 29929-29937.

Wang, P. K., 2003: Moisture plumes above thunderstorm anvils and their contributions to cross-tropopause transport of water vapor in midlatitudes. *J. Geophys. Res.*, **108(D6)**, 4194, doi:10.1029/2002JD002581.

Yang, P., and K.-N. Liou, 1998: Single scattering properties of complex ice crystals in terrestrial atmosphere. *Contr. Atmos. Phys.*, **71**, 223-248.

Zender, C. S. and J. T. Kiehl, 1994: Radiative sensitivities of tropical anvils to small ice crystals. *J. Geophys. Res.*, **99**, 869-880.

Figure Captions

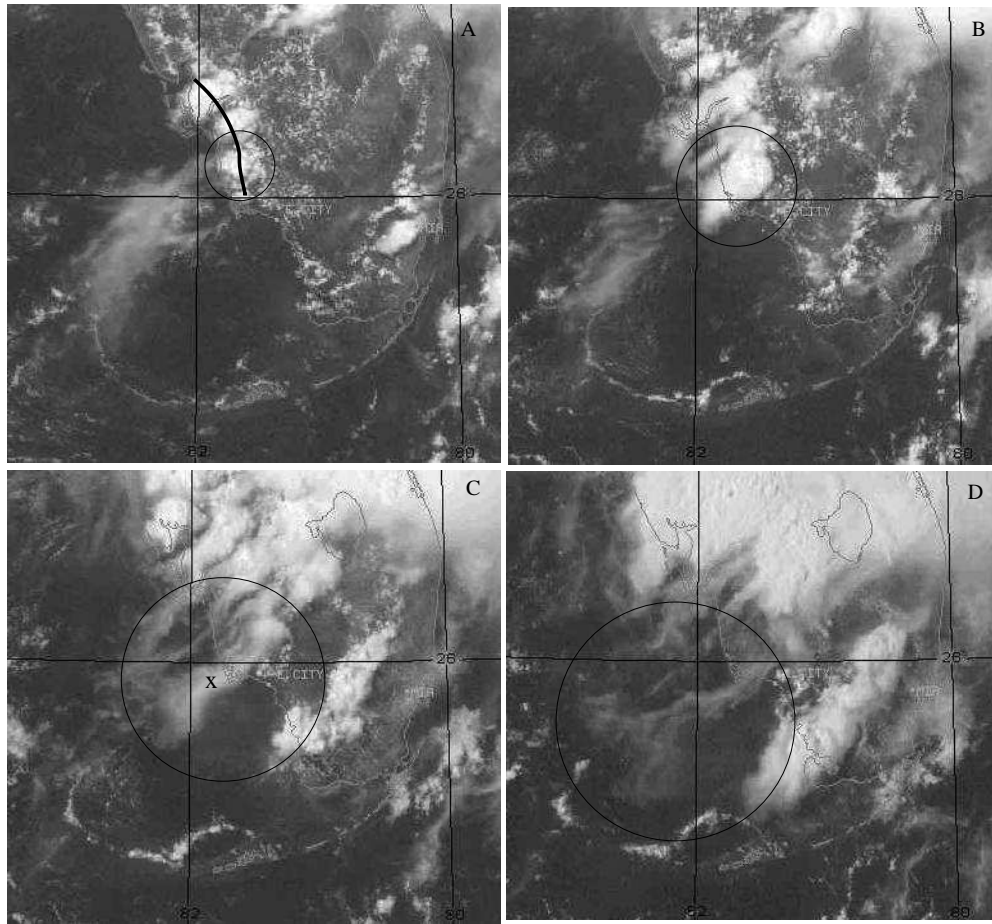


Figure 1. Visible GOES-8 satellite images over Southern Florida for the period of 1745 UTC (A) to 2045 UTC (D) in one hour increments. The circle denotes the storm/anvil of interest. The thick line in (A) marks the location of the sea-breeze front, which caused the low-level convergence that generated the storm. The 'x' in (C) denotes the approximate location of the spiral ascents completed by the aircraft.

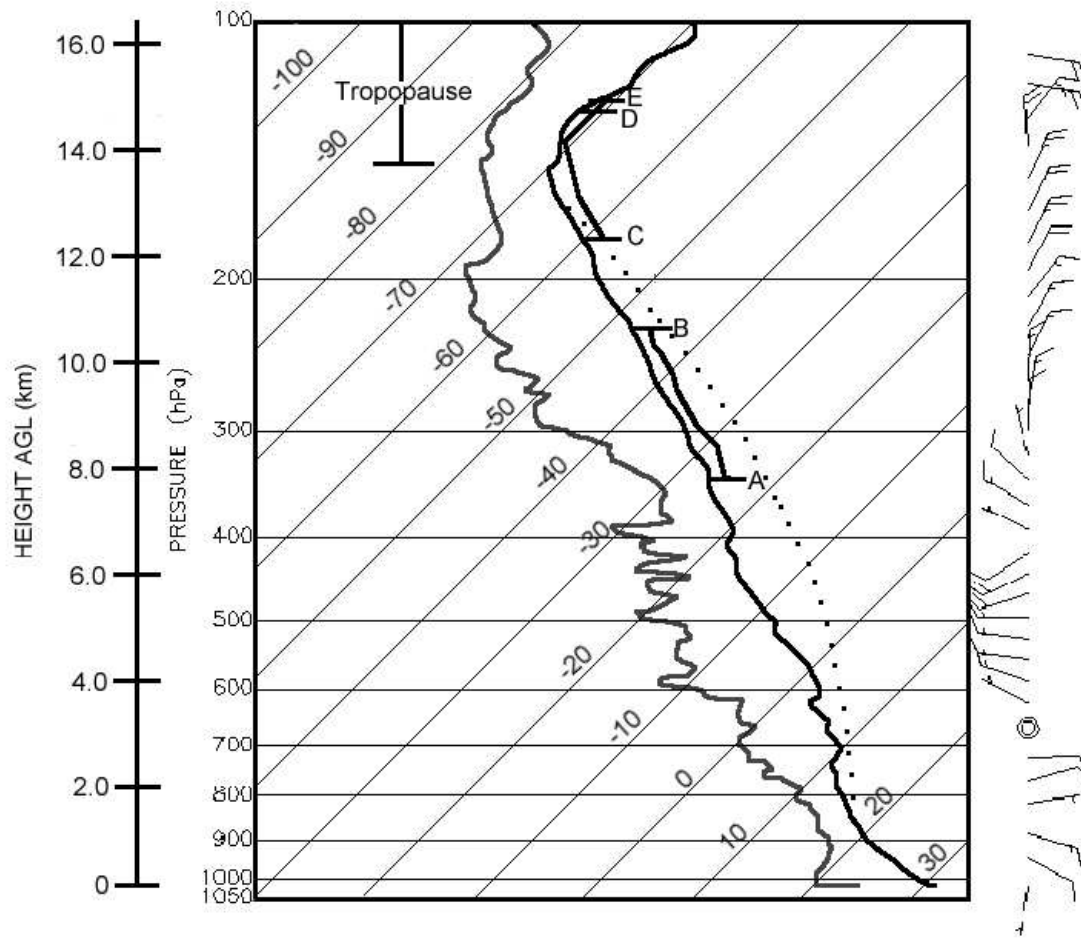


Figure 2. Skew-T, log (P) diagram of a temperature (black) and dewpoint (gray) sounding taken at $25^{\circ}53'N$ $81^{\circ}19'W$ at 1725 UTC on 21 July 2002. Heavy lines to the right of the temperature profile denote temperatures observed during vertical profiles by the NASA WB-57F and UND Citation during a profile through thin tropopause cirrus and a cirrus anvil. Approximate height, using a scale height of 7.2 km estimated from raw height coordinates from the radiosonde, is shown to the left of the pressure scale. A denotes the base of the anvil, B the top of the anvil, and C and D the base and top of the thin tropopause cirrus, respectively. E denotes the maximum height of the WB-57F during the vertical profile. The dotted line represents saturated surface parcel ascent for $\theta_e = 296$ K.

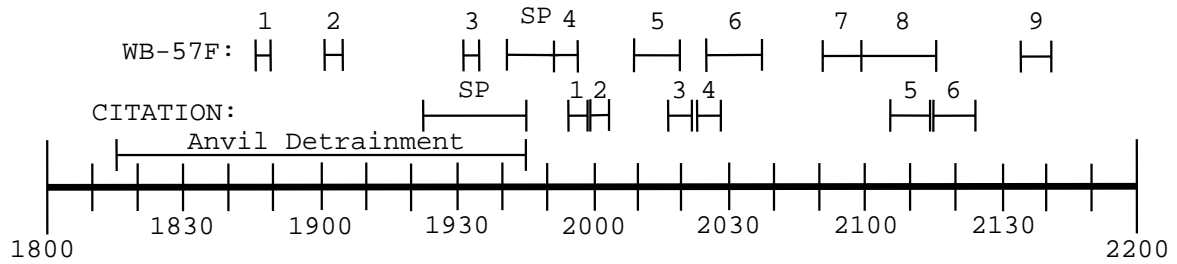


Figure 3. Time-line (in UTC) of the numbered flight legs completed by the NASA WB-57F and UND Citation on 21 July 2002 while sampling the evolution of an individual anvil (Fig. 1). *SP* refers to the spiral vertical profile completed by each aircraft. The period associated with detrainment of the anvil from the storm is estimated from GOES-8 satellite imagery. The anvil detached from the storm at 1945 UTC. Initial development of the storm occurred at approximately 1650 UTC.

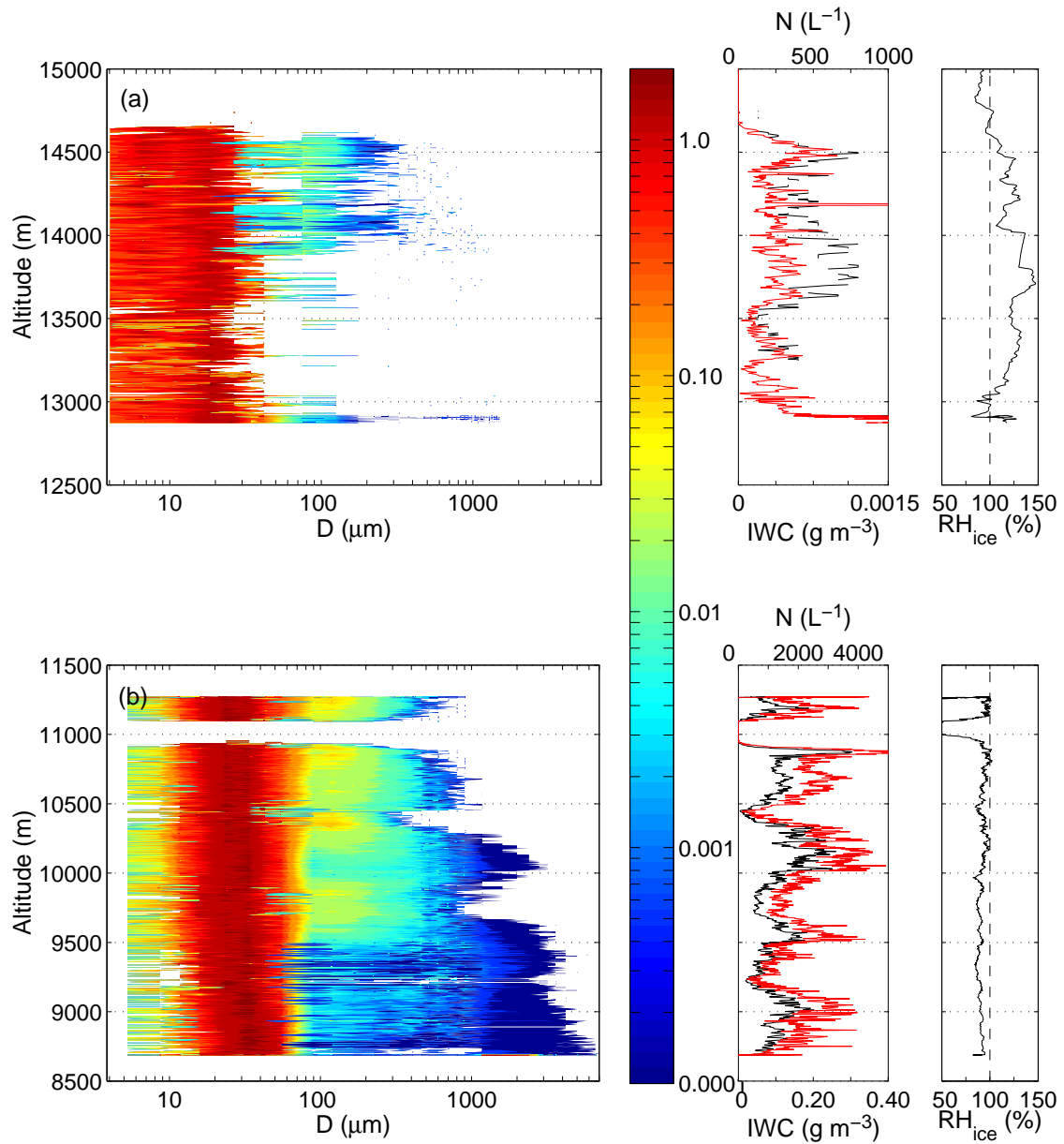


Figure 4. Vertical profile of size distributions normalized by total concentration ($((dN/d\log D)/N)$), total cloud crystal concentration (N) (red line), ice water content (IWC) (black line), and relative humidity with respect to ice (RH_{ice}) in the thin tropopause cirrus (a) and anvil (b) sampled by the WB-57F and Citation, respectively, on 21 July 2002.

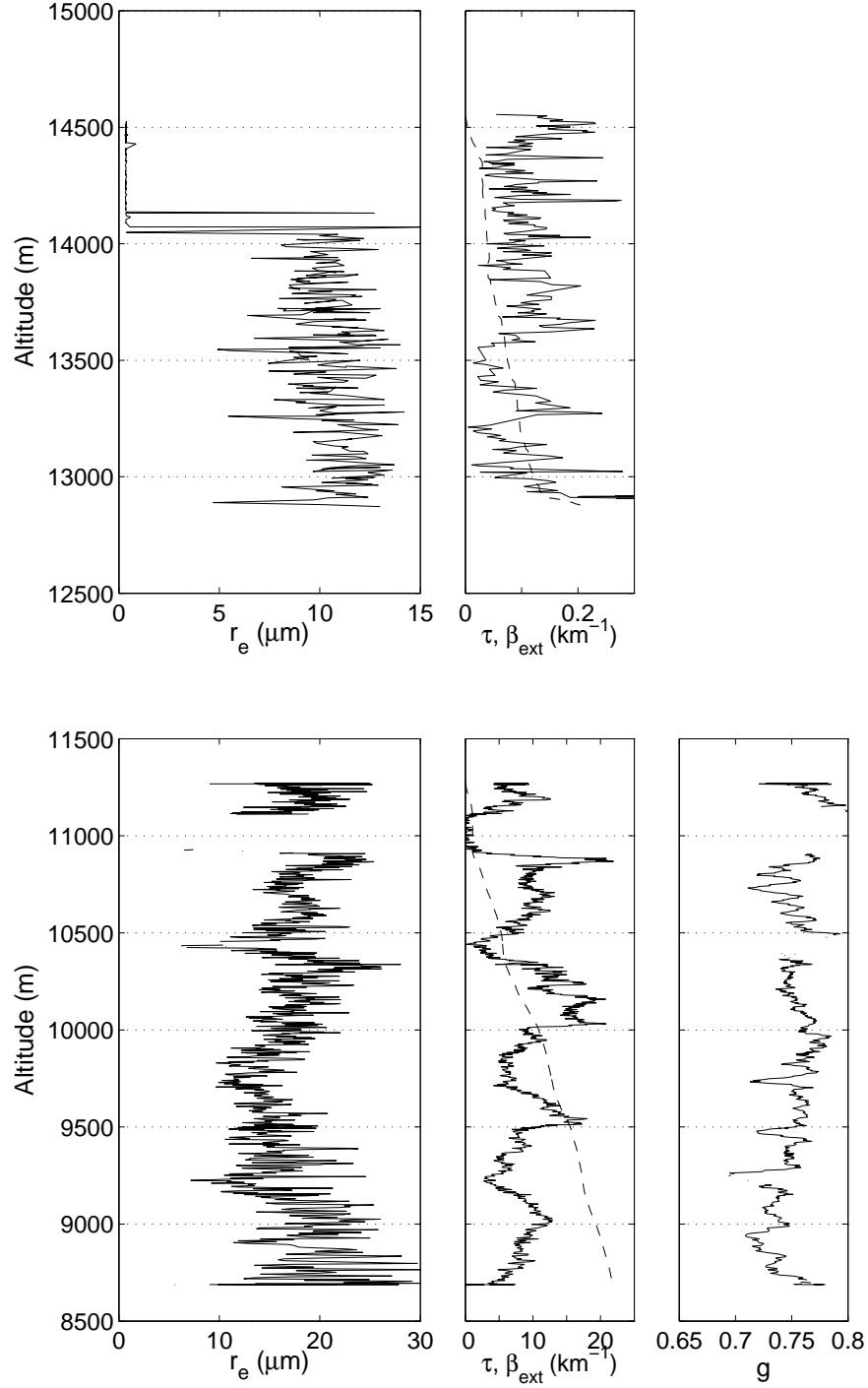


Figure 5. As for Fig. 4, but effective radius r_e , visible extinction β_{ext} , accumulated visible optical depth τ measured from cloud top (dashed), and asymmetry parameter g . Effective radius, extinction, and optical depth plotted in upper panels are derived from the CAPS probe. Measurements in lower panels are derived from the CVI and CIN probes. τ is derived from vertically integrating β_{ext} .

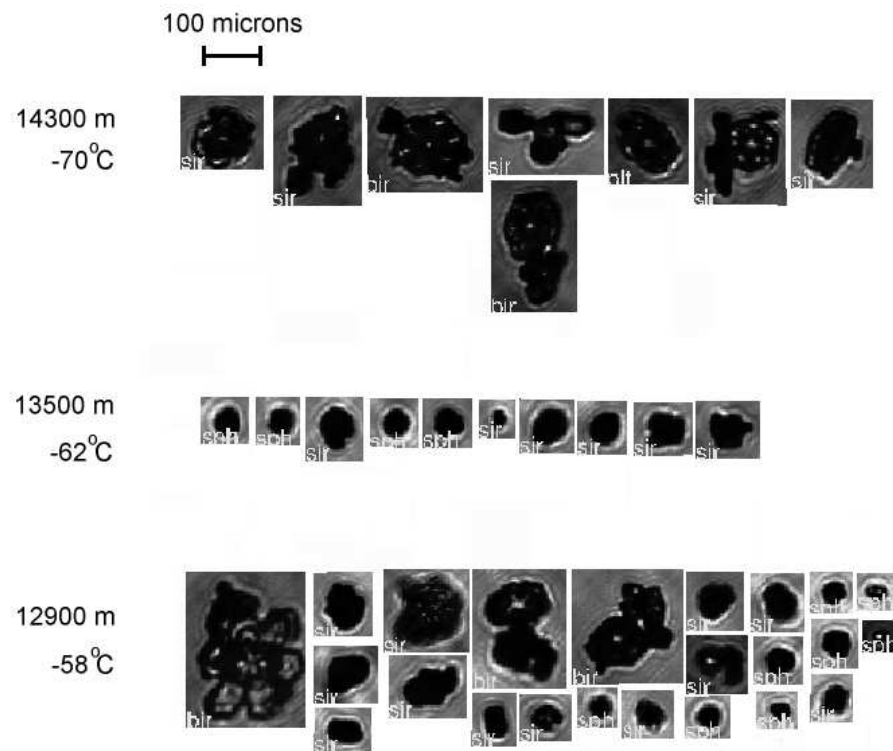


Figure 6. CPI images of crystal habits encountered during the WB-57F vertical profile within the thin tropopause cirrus.

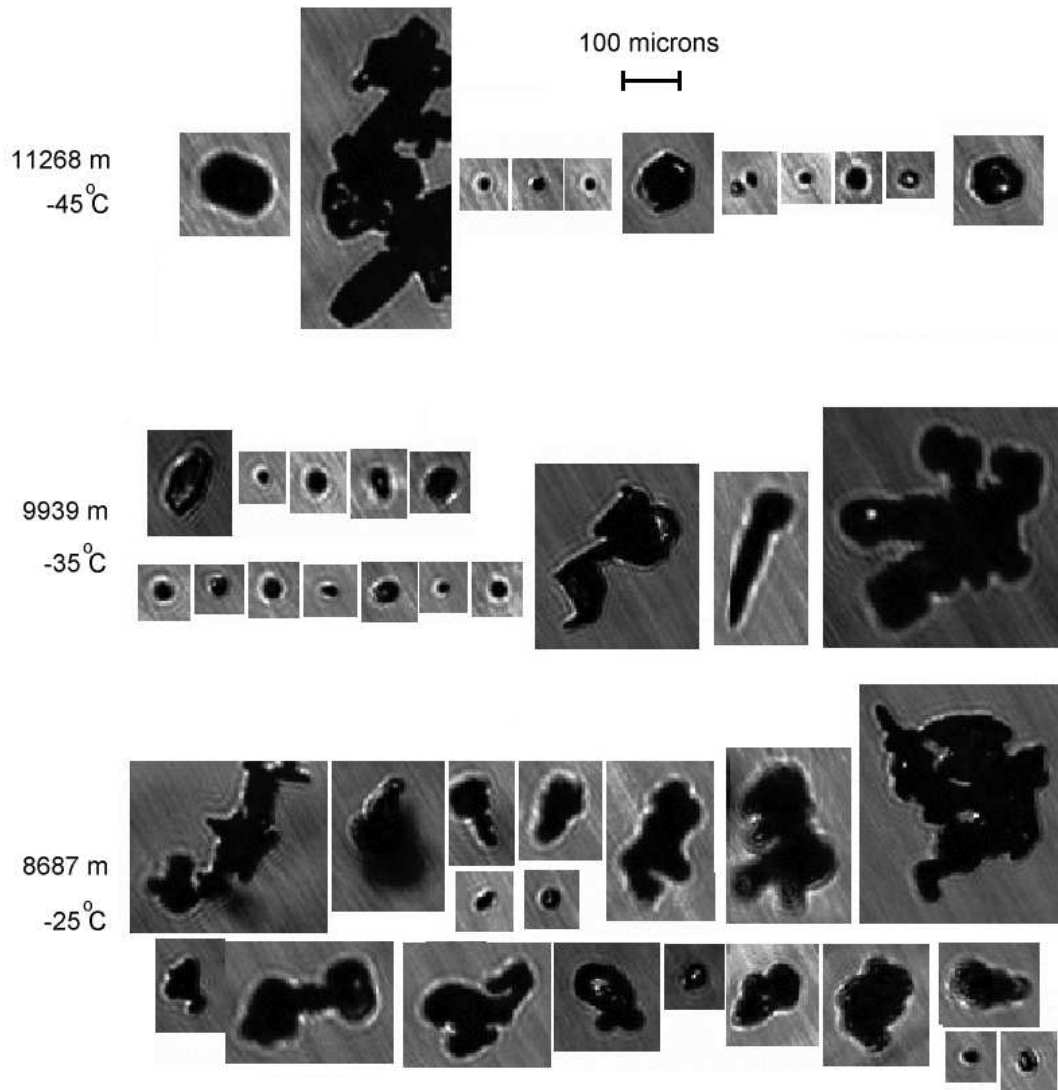


Figure 7. CPI images showing the crystal habits encountered during the Citation vertical profile within the anvil.

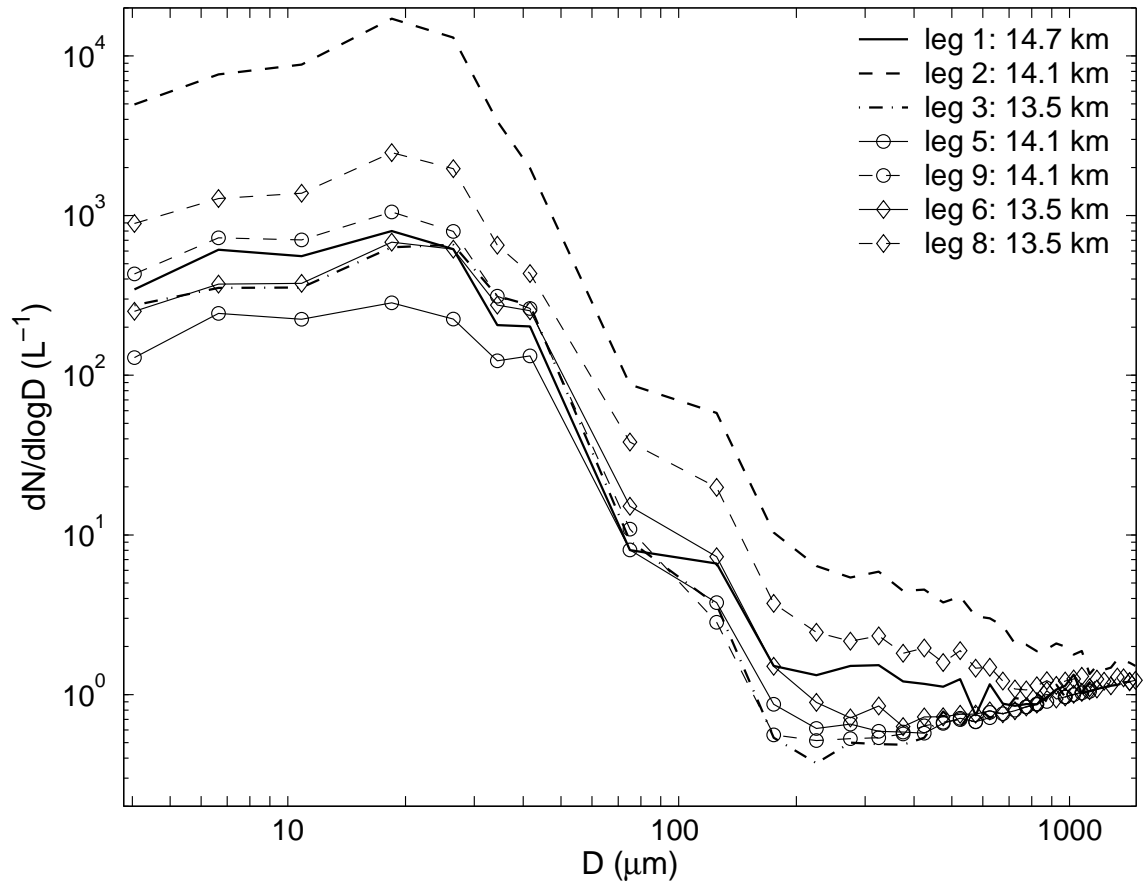


Figure 8. Average ice crystal size distributions near the tropopause 20 km downwind from a convective impulse that reached its peak at 1840 UTC. Measurements were obtained aboard the WB-57F during legs 1 to 3 (Fig. 3).

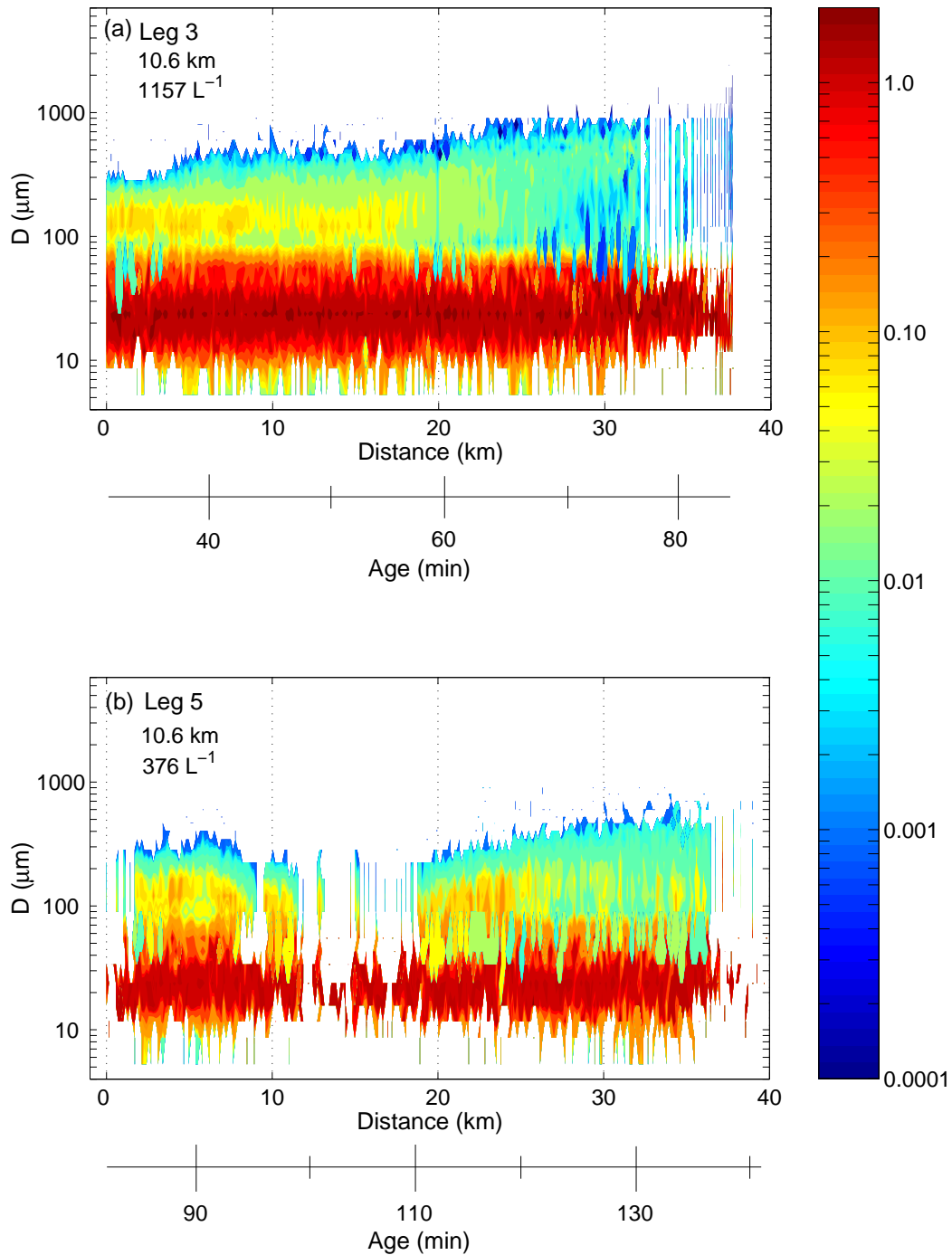


Figure 9. Normalized ice crystal size distributions $((dN/d\log D)/N)$ within the anvil during Citation legs 3 (A) and 5 (B) at 10.6 km altitude. The time-line on the bottom represents the estimated age of cloudy air since initial detrainment from the convective updraft. Average altitude and concentration are shown in the upper left corner of each plot. Distance is measured from the upwind to the downwind edge of the anvil.

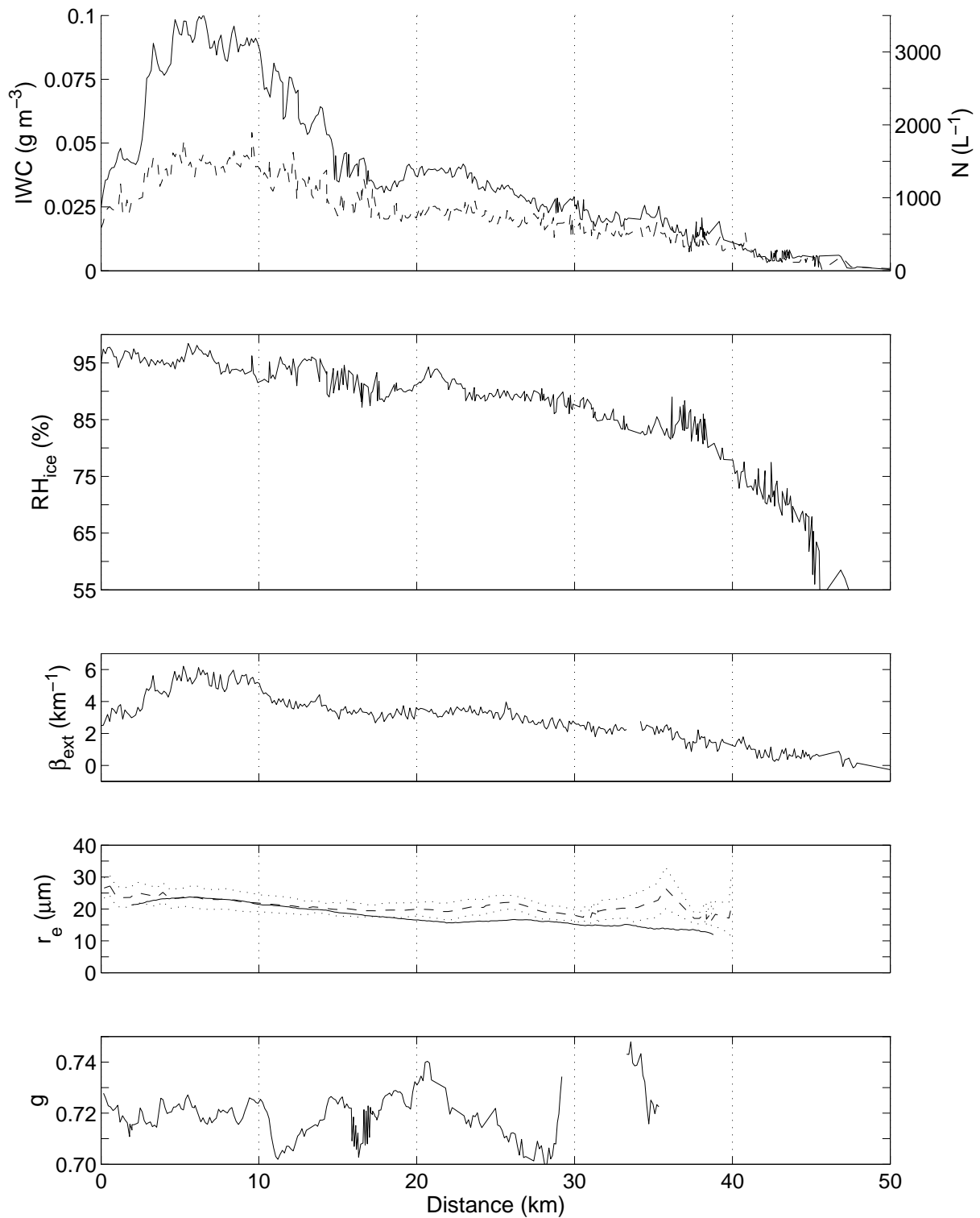


Figure 10. Citation measurements of anvil ice water content IWC (solid line) and ice crystals number concentration N (dashed line), relative humidity over ice RH_{ice} , extinction coefficient β_{ext} , effective radius r_e , and asymmetry parameter g , averaged over legs 1 to 6 (Fig. 3). GOES-8 retrievals of r_e (dashed lines with dotted uncertainty; defined according to Eq. 1) are shown for comparison alongside measured values (solid lines). Distance is referenced from the up-wind edge of the anvil.

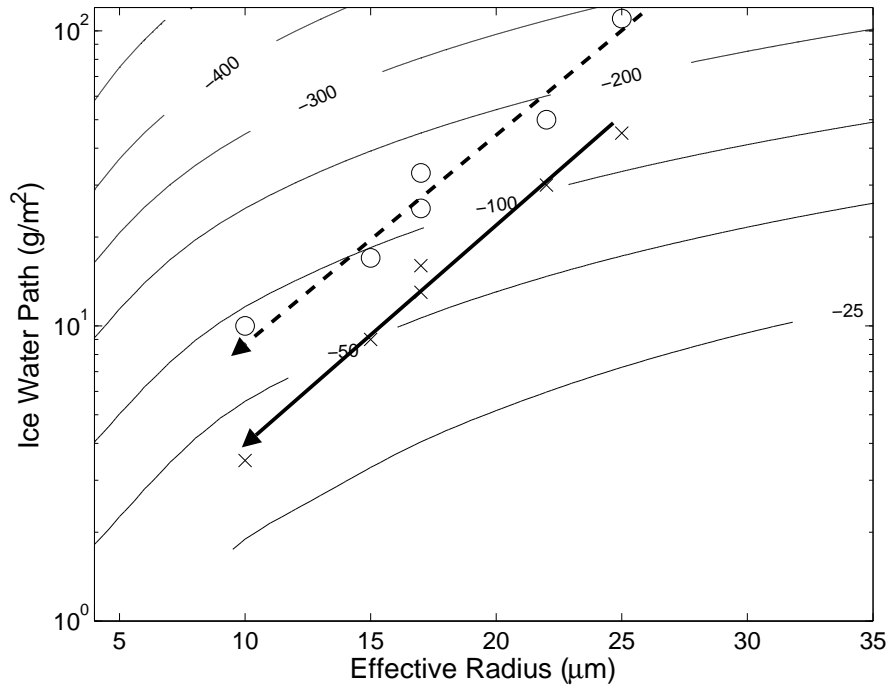


Figure 11. Top of tropopause net cloud radiative forcing calculated for the 21 July anvil-TTC system at 2024 UTC (contours, W m^{-2}) as a function of the ice water path and effective radius of the anvil. The dashed arrow represents the calculated CRF_{net} trend when using only the *in situ* anvil r_e and anvil IWC measurements (circles) from the Citation (leg 3), assuming a cloud depth of 500 m. The solid arrow represents the measured CRF_{net} trend when using only the measured CRF_{net} from the WB-57F (leg 5) and *in situ* anvil r_e (crosses, Citation leg 3). For each case, symbols are separated by 5 km of horizontal flight.

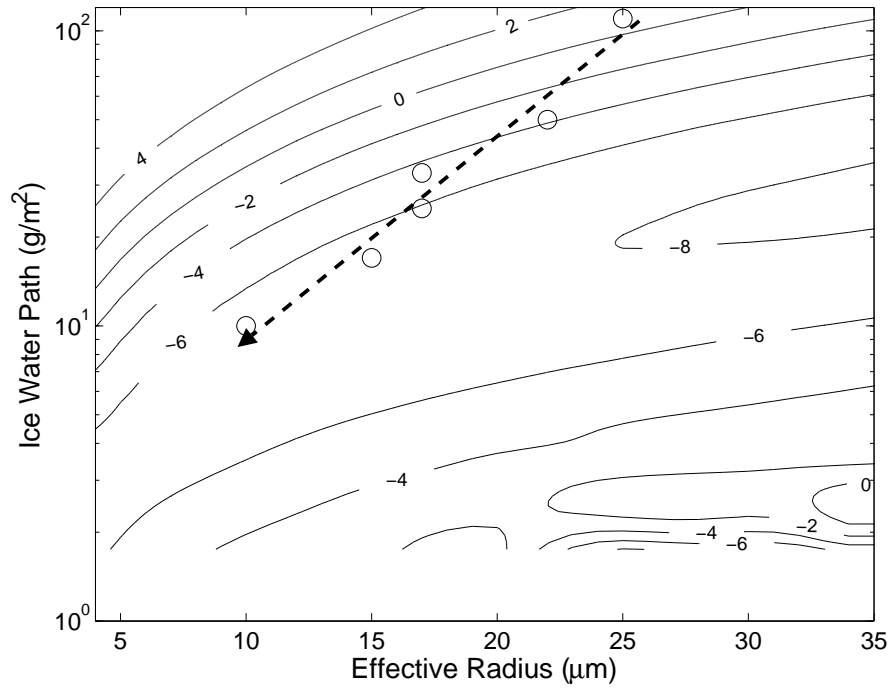


Figure 12. As for Fig. 11, except the contribution of the TTC cloud to total forcing by the TTC-anvil system.

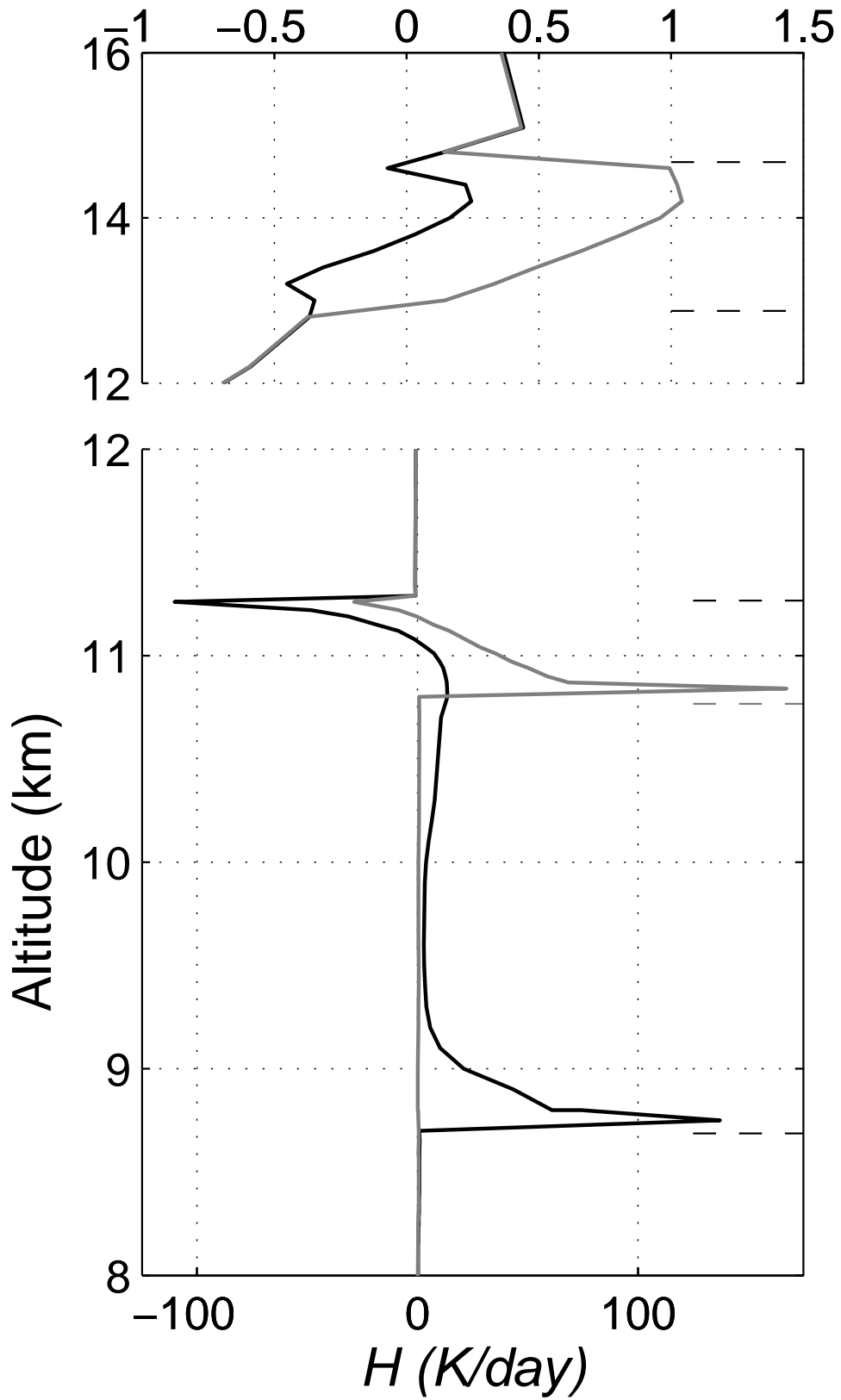


Figure 13. Calculated heating rate profiles for an anvil attached to the convective core ($\tau = 21$ and $r_e = 20\mu\text{m}$; black line), and thin anvil cirrus detached from the core ($\tau = 2$ and $r_e = 12\mu\text{m}$; gray). Dashed lines indicate cloud boundaries of the TTC (upper panels) and anvil (lower panels).

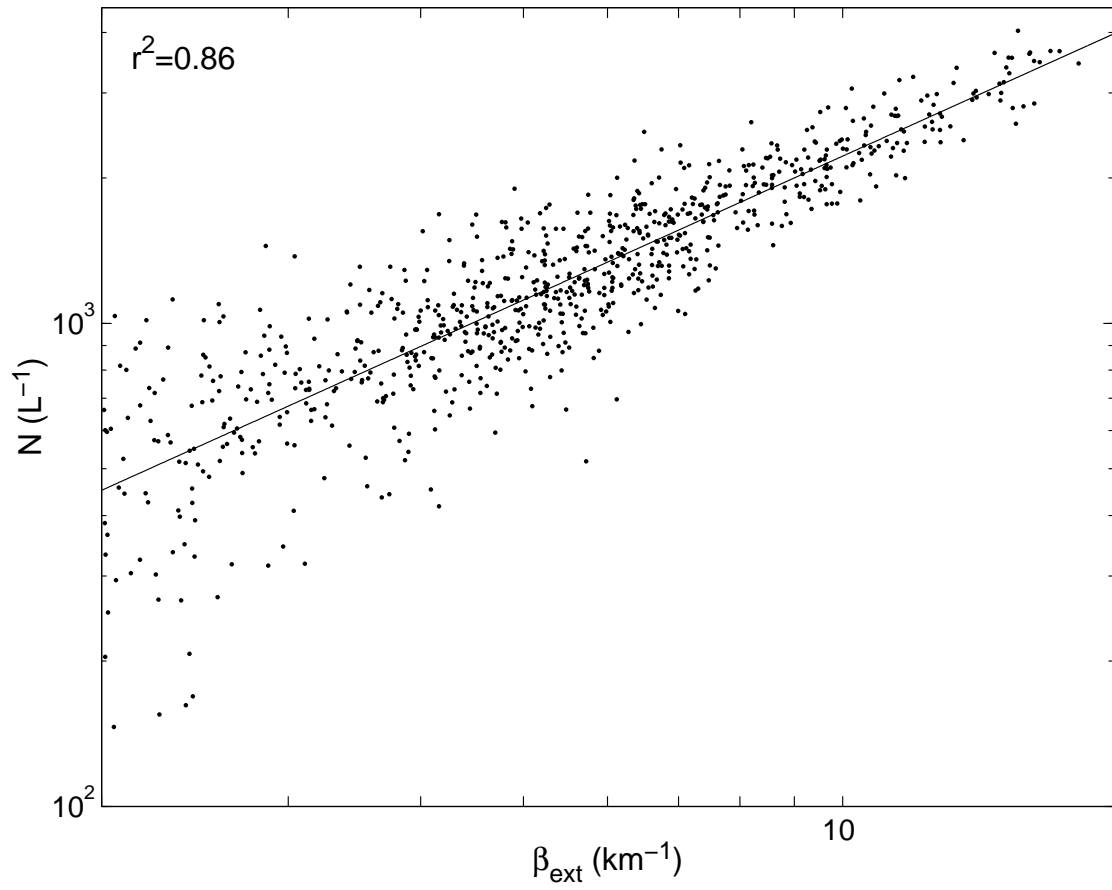


Figure 14. 1 Hz measurements of β_{ext} and N for all six Citation legs through the anvil. The solid line is the least squares fit $N=227\beta_{\text{ext}}^{0.99}$.

Tables

Table 1. Leg-averaged altitude, age, temperature, total concentration (N), ice water content (IWC), relative humidity (RH), effective radius (r_e), and visible extinction coefficient (β_{ext}) measured by the NASA WB-57F within the thin tropopause cirrus (TTC). Legs 1, 2 and 3 were flown across wind while the anvil beneath the TTC was still forming. Legs 5 and 9 and legs 6 and 8 were flown along axis. Age is calculated relative to the time of initial detrainment of the anvil proper from the convective updraft. Standard deviations in the measurements are shown in parenthesis. Average values below the detection threshold are indicated by a dash. IWC , β_{ext} and r_e were measured by the CIN and Harvard water probes.

	Across TTC Axis			Along TTC Axis			
Leg	1	2	3	5	9	6	8
Altitude (km)	14.7	14.1	13.5	<u>14.1</u>		<u>13.5</u>	
Age (min)	*	*	*	74	126	92	116
Temperature ($^{\circ}\text{C}$)	-70	-67	-63	-68	-67	-63	-62
N (cm^{-3})	0.57 (0.54)	10.7 (8.8)	0.40 (0.39)	0.79 (0.53)	0.17 (0.20)	0.59 (0.68)	1.24 (1.10)
IWC (mg m^{-3})	1.6 (1.1)	35 (30)	2.3 (1.2)	1.8 (0.9)	0.5 (0.5)	1.8 (1.6)	4.4 (4.2)
β_{ext} (km^{-1})	0.5 (0.6)	9.0 (7.1)	0.4 (0.5)	0.4 (0.3)	-	0.4 (0.5)	0.8 (1.0)
r_e (μm)	3.8 (2.1)	7.3 (3.4)	5.0 (1.5)	5.9 (1.6)	5.8 (0.8)	5.5 (3.3)	7.4 (2.2)
RH_{ice} (%)	98 (9)	118 (10)	124 (11)	119 (5)	116 (7)	112 (7)	117 (10)

Table 2. Leg-averaged altitude, age, temperature, total concentration (N), ice water content (IWC), relative humidity (RH), total water content (ice plus vapor) (TWC), effective radius (r_e), visible extinction coefficient (β_{ext}), and asymmetry parameter (g) measured by the UND Citation within the anvil. Age is calculated relative to the time of initial detrainment from the convective updraft. Standard deviations in the measurements are shown in parenthesis. Average values below the detection threshold are indicated by a dash.

Leg	1	6	3	5
Altitude (km)	<u>11.2</u>		<u>10.6</u>	
Age (min)	35	123	58	117
Temperature ($^{\circ}\text{C}$)	-45.3 (0.1)	-44.9 (0.1)	-39.9 (0.2)	-39.5 (0.1)
θ ($^{\circ}\text{C}$)	70.6	70.8	69.1	69.5
U, V (m s^{-1})	3.8, 4.2	6.2, 6.2	1.8, 2.3	2.3, 3.8
RH_{ice} (%)	101 (8)	92 (6)	104 (5)	93 (8)
TWC (mg m^{-3})	122 (24)	68 (5)	220 (54)	152 (27)
IWC (mg m^{-3})	55 (21)	5 (3)	95 (53)	23 (23)
N (cm^{-3})	1.3 (0.5)	0.23 (0.13)	1.6 (0.6)	0.47 (0.36)
r_e (μm)	12.7 (4.2)	-	17.9 (8.0)	16.8 (7.5)
β_{ext} (km^{-1})	7.1 (2.0)	-	8.6 (3.6)	3.0 (1.6)